uc3m | Universidad Carlos III de Madrid

University Degree in Aerospace Engineering
2018/2019

Bachelor Thesis

Experimental Testing of a Wake Ingesting Propeller

Manuel Arán Tejada

Tutor
Marco Raiola
EPS Leganés, March 2019

1 Abstract

The aviation industry is rapidly changing, lead by a growing demand on more modern aircrafts who are able to address the future challenges in terms of fuel consumption, efficiency and green emissions among other factors. In order to correctly address these challenges, new technologies and non-conventional designs are being investigated upon. One of the phenomena which could be taken advantage of is the Boundary Layer Ingestion (BLI). Such phenomena take place whenever the propulsive system ingests an airflow which has been modified from the freestream conditions, either containing boundary layer flow from near aircraft features, or the more developed wake of a body. The aim of this paper is to gain a deeper insight on the parameters governing such phenomena. For such purpose, an experimental parametric study of a propeller performance ingesting the wake of three spheres at three different distances between them will be carried out on a closed loop wind tunnel. Results show that the distance between the propulsive unit and the bodies does not produce performance differences on the advance ratios range considered. However, the sphere size does produce changes on the system performance, either by increasing the produced thrust, or by decreasing the consumed power. The performance improvement mechanism is observed to depend on the sphere non dimensionalised size with the propeller diameter. For smaller spheres, a power reduction is observed, while for bigger ones thrust enhancement is produced.

2 Key Words

Propeller, experimental, wake ingestion, WI, boundary layer ingestion, BLI, propulsion, sphere.

3 Acknowledgements

First, I would like to thank my mentor Marco Raiola for his patience and all the counselling he provided me all along this thesis, from scratch to the last comma of this paper.

Next, thanks to Carlos Cobos, whose experienced advice during the set-up design was most appreciated.

Last but not least, my most deep and kind thanks to my family, who gave me unconditional support during these months, as well as lifting me up when I was on the floor. I would like to specially dedicate this thesis to my father. Without him, I wouldn't be who I am.

Contents

List of Figures

4 Preliminary Considerations

4.1 Introduction

Since the dawn of History, humankind has always looked in reverence to the skies, not only to the unreachable at first stars, but also to the creatures which were able to freely roam the firmament. The ability to fly has always been present in the dreams and desires of all humans, and as such there are records of several myths and legends, from Icarus in the Ancient Greece to the half bird half human deity Garuna, from the Hindu mythology. However, the desire of flying was not only restricted to the legends, as scientific research with an acceptable degree of rigorousness is traceable back to approximately 1000 B.C., when the Chinese developed the kite technology, starting the *lighter-than-air* vehicles development.

However, it was not since the the end of the 18^{th} century, with the french hot air balloon flights, and the beginning of the 19^{th} one, with the development of the rigid wing concept by Sir George Cayley (father of the *heavier-than-air* aircraft technology) that the invested efforts began to yield significant results. Finally, the process of developing a light enough power plant culminated with a milestone which would start the *powered-flight* aircraft era on the 17^{th} December 1903, with the iconic first flight of the Wright Brothers in North Carolina, USA [1].

Since that date, nearly 115 years ago, aviation and its associated technologies have become has become one of the scientific and engineering cornerstones of our society, where state-of-the-art discoveries are achieved on a regular basis. From composite materials to novel electronic and communications technologies, applications of the actual aerospace industry are almost endless. One of those contributions take place in the propulsion field. Since the beginning of aviation, how to efficiently provide the aircraft with a power source to allow for autonomous movement has been one of the main challenges in the aeronautical engineering field. Solving the propulsion problem for the aircraft design delayed the aviation progress in its early stages, as no power plant gave the necessary power-to-weight ratio suitable for this applications. Some years needed to pass as enough research allowed for the appearance of the first internal combustion engines. This kind of engines were couple with one device which was found on every aircraft back then, and is still used nowadays: the propeller.

A propeller may be understood as a highly twisted wing, whose usually variable cross-sections closely resembles that of a wing, in addition to a much thicker part of it near its root (hub) for structural reasons, with sharp trailing edges and relatively rounded leading edges [2]. In fact, many propellers cross sections are designed based on widely spread airfoils. Though simple upon its concept, designing and manufacturing an efficient propeller has proven to remain a challenging engineering problem over the years. Usually, its design is based on the mission characteristics it (or the aircraft upon which it will be attached to) will perform, such as cruise velocity, rotational speed or whether it will be a fixed or variable pitch propeller. Despite the fact that such technology suffered a drop in popular-

ity with the debut of the modern turbojet engines, it recently has regained adepts thanks to the UAVs (Unmanned Aerial Vehicle) proliferation and development of new materials and systems not available back then, such as more advanced plastic materials or BLDC motors. Under these new circumstances, the propeller shows itself as the appropriate propulsion system for smaller aircrafts with specific mission profiles.

4.2 Socioeconomic Environment

At the current moment, the commercial aviation industry and market are entering a stage for major growth, especially in the emerging economies, while a less impressive yet steady development will take place in the already established (maturing) markets (North America and Western Europe). As such, the FAA (Federal Aviation Administration) is expecting in the USA territory the total mainline air carriers RPM (Revenue Passenger Mile) to grow at an average annual rate of 2.7%, with flight total operations increasing at a steady average annual rate of 1.0% until 2034 [3]. As stated before, this growth tendency is not only attributed to the USA or Northern America market. In 2010, Airbus group also predicted that the air traffic would double by 2025, with a world annual growth of 4.5%. Both statements made by comparing the actual RPK (Revenue Passenger Kilometer) with the predicted one. In addition, Airbus distinguishes between the maturing regions (Western Europe, North America, Japan and Australasia) with an annual RPK growth of 3.7%, and the expanding (emerging) regions, which account for China, India, Middle East, Asia, Africa, Commonwealth of Independent States, Latin America and Eastern Europe, with an annual RPK growth of 6.1% [4].

A closer look performed by the European authorities on its own market reveals four possible scenarios. Nevertheless, though these scenarios are conceptualised with scope on such market, any change in a mature market such as the European will surely influence to a certain degree the rest of matured markets, as well as the emerging ones. First of all, a *Global Growth* case is predicted, with a strong global growth fused with technological improvements directed to mitigate arousing environmental concerns (i.e. reduction of greenhouse gas emissions). Afterwards follows the *Regulation and Growth* most likely scenario, where a regulated market growth is set to equilibrium between the increase in air traffic growth with the environmental concerns. The third scenario would be a *Happy Localism*, where the European air traffic market is mainly directed inside its geographical limits (increase in the growth for the European travel, decrease in the growth for international travel). Finally, an unlikely *Fragmenting World* scenario is taken into account, where barriers to free trade increases. All in all, the least dynamic scenario (the one which would imply a lower growth) would be the *Fragmenting World* scenario, with a 12% European air traffic increase (2040 levels compared to 2017), while the most optimistic case would be the *Global Growth* scenario, with a forecasted increase in the air traffic of a 84%. This figures of merit are based on the annual number of flights. On the other hand, an additional remark regarding the unmanned aerial systems (UAS, also known as 'drones') is stated, where the

commercial flights regarding these aircrafts could increase from 6 flights/day to almost 100 by the end of 2040. However, the lack of consensus about the UAS increasing applications, its unclear growth rate due to legal issues [5] and the definite possibility of them taking over short and medium haul freight flights make this figures a low and weak estimation [6].

These growth figures are confirmed by IATA (International Air transport Association) as reported in its 2018 annual review report, referring to 2017 results. A 8.1% industry-wide RPK increase was detected with respect of 2016, which indicates a strong demand increase. Taking a closer look to the air traffic data, the most dynamic market was the domestic Chinese market in regard to O-D journeys (Origin-Destination), with and addition of 59 million flights compared to 2016, which represents an increase of 14.7%. The domestic markets of United States and India completed the podium, with increases of 4.7% and 17.6% respectively. This data is coherent with the models which forecast a continuous growth of the air carriers market, specially in the Asian emergent niche. This is further confirmed by the words of Goh Choon Phong, Chair of the IATA Board of Governors & CEO of Singapore Airlines: "*If you look at projections, by 2036 there will be 7.8 billion people travelling, almost half of them to, from and within Asia-Pacific*" [7]

To sum up, a steady growth is expected in the air travel market, with a lower rate in the already matured markets and great room for increase in the emerging ones, with special regards to the Pacific-Asian niche. In order to match the increasing demand, companies, organisations and countries are actively engaged in promoting new technologies, infrastructures and legislation to suitable for the incoming years and the challenges which will bring.

European authorities, lead by the European Commission, depicted the efforts European aviation should exert in order to give a proper answer to the forecasted growth and expected challenges, which would bring major changes in different fields such as safety standards, airport structures, aircraft technologies and regulations. Thus, efforts are expected to be focus (among others fields) on achieving and maintaining technological leadership across the aviation industry, as well as reducing aviation impact on citizens and environment (through noise and greenhouse gas emissions reductions). In other words, European aviation vision for the incoming years goes through offering the best aeronautical products and associates services, as well as protecting the environment, including the investigation of alternative energy sources along with sustainable energies [8].

These goals, which identifies with two of the 5 main challenges established by ACARE (Advisory Council for Aviation Research and Innovation in Europe) in its Strategic Research and Innovation Agenda (SRIA), are further split in concise action areas: develop the air vehicles of the future (both by evolutionary and revolutionary approaches), increase the resources use efficiency (which translates into improving fuel efficiency) and understanding aviation impact on climate and environment (as well as regulating accordingly [9]. The last action areas are directed towards the Flightpath goals of reducing CO_2 emissions by 75% and NO_x by 90%.

In a parallel investigation line, new technologies should allow for a noise reduction of a flying aircraft of 65% (compared to 2000s aircrafts noise levels) [8].

Similar goals are established by the USA authorities, which were established by the NASA N+3 program, including a 75% reduction in NO_x emissions and a 70% fuel burn reduction, with reference to the CAEP 6 standards (Committee on Aviation Environmental Protection, 2004 version) established by ICAO. Such goals are to be achieved among others by the year 2035 and may not be seen as isolated goals, but rather the result of the continuous improvement considered in the earlier N+1 and N+2 programs. Noise reduction goals are also introduced [10].

4.3 State of the Art Technologies

In order to achieve these ambitious goals, one of the key solutions goes through the development of novel technologies and designs, focused towards the construction of more efficient aircraft which would provide the expected load factor to the growing demand. More efficient aircrafts will allow for a reduction in the greenhouse gas emissions (as less fuel would be required to be burnt for a given mission). One of these revolutionary concepts goes through a closer integration of the different systems an aircraft is composed of, with special attention to the integration between the propulsive elements of the aircraft (from the usual jet engines to counter rotating propellers) and its fuselage. However, this integration conveys numerous problems. On one side, there is a need for a new theoretical analysis development, as the classical approach makes difficult to asses the different forces taking part in a relatively closely integrated aircraft. On the other hand, such an integration imposes the superposition of several physical phenomena whose combination has not been studied before (i.e. vibration issues). Such new technologies which are currently being researched upon include advance structural and engine materials, high aspect ratio wings able to attain laminar flow, active load alleviation, reduced secondary structure weight, trussed wings, high bypass ratio engines ($BPR \approx 20$) and variable area nozzles [11].

Upon these technologies and integration issues, one of phenomena the new aircraft design could take advantage of is the Boundary Layer Ingestion (BLI) or Wake Ingestion (WI). This phenomena happens whenever the propulsive system intake ingests a modified flow, either containing part of the airframe boundary layer or another aircraft component wake. This concept is in direct opposition with the traditional design approaches, where it is preferred that the propulsive system receives the freestream air flow. This phenomena has been theoretically predicted to increase the performance of the propulsive system as earlier as Betz [12], thanks to its work on ducted propellers, and further investigated upon by Smith work [13]. As will be developed later, this is due to the flow momentum deficit at the intake plane, which enables for a lower power need in order to impart the fluid with the same momentum difference (between intake and outlet plane) for the freestream case. According to [13], savings could add up to 50% for some cases.

However, despite the theoretical support to the idea of this saving mechanism, there still remains many unknowns with the quantification of the saving mechanism, as well as its functioning on real scale prototypes due to the complex problems arousing when implementing theoretical models in the flow surrounding a moving part (be it a fan, propeller, compressor,...). As a consequence, some examples in the literature may be found centered not only in the development of an accurate model able to describe the problem, but also in the set up and testing of different configurations which attempt to shred more light on the power saving mechanism. Theoretical approaches usually follow either the exergy concept or power balance method, with the latter thoroughly developed by Drela [14] in the late 00's, and and further polished by Arntz et al. [15] to include thermal dissipating terms, thus achieving a formal exergy model applicable to the aircraft. Nevertheless, the exergy concept could be traced back to the first steam engines [16], yet it was not up to 1956 that Rant [17] first came up with the term. This methods will be further explained later in Subsection 5.

Numerical approaches as well as experimental set-up performed by Lv et al [18] and [19] stated additional theoretical background, as well as up to 18% shaft power reduction for the BLI case by setting an streamlined body before an unducted propeller in an open wind tunnel. On the other hand, Uranga et al. [20] reported a mechanical flow power reduction of 8.6% when analysing a 1:11 scale of the D8 concept aircraft at an open wind tunnel. In addition, a fuel burn reduction of between 3 to 5 % was found when analysing the BLI proposal for the a Hybrid Wing Body Aircraft [21] by using numerical simulations. On the other hand, Arntz et al. [22] performed as well numerical simulations on a 2D simplified representation of a wing body aircraft, showing that an improvement of the overall performance up to 50% is possible (in terms of propulsive exergy change) in addition with an accurate control of the airframe temperature. Moreover, G. de Oliveira [24] developed a more general model of the influence of an axisymmetric body upon an actuator disk, proving than a thrust increase is possible for the same power levels when compared with a freestream case. The validation was executed comparing analytic results and numerical analysis, showing good agreement in between.

The aim of this paper is to continue the research upon the Wake Ingestion (WI) and Boundary Layer Ingestion (BLI) phenomena. First of all a theoretical model will be presented, based on the one developed by Drela [14], aimed at correctly assessing the power sources and sinks along the propeller performance. Afterwards, a experimental set up will be derived and explained for the open and closed wind tunnel facilities at Universidad carlos III de Madrid. Through these experiments, the optimal distance in between a bluff body (sphere) and the propulsion system (two blades propeller mounted on a BLDC motor) for minimizing the power consumption will be looked for, as well as the derivation of the main parameters affecting the propulsive system performance. Those parameters will be varied, and their influence assessed and discussed. On the other hand, the flow velocity field downstream the propeller will be described, in order to analyze the energy conversion mechanism between the wake excess (or defect) energy and the viscous dissipation terms.

First of all, the applied method for this paper will be presented. On one hand, it will include the theoretical layout (*Section 5*) supporting the results analysis, which is formed by a brief outline of the propeller theory (*Subsection 5.1*)and the power balance method description (*Subsection 5.2*). On the other hand, the experimental set up built for the concerning experiment will be accounted for in *Section 6*. The design and manufacturing process of the set up for both the open and closed loop wind tunnels is presented in *Subsections 6.1 & 6.2*. The electronic equipment employed on the measurement procedure will be listed and their characteristics concisely developed, as well as some theoretical background. Next, the error analysis of the results, as well as some necessary wind tunnel corrections will be outlined. An inventory of the used parts will be available (*Appendix A*), as well as the tailored pieces blueprints (*Appendix B*). analogously, the final project budget for this experiment is shown in *Subsection 6.6*. Next, the results and the discussion of some cases of interest will be shown in *Chapter 7*, though a list of all the obtained performance curves is given in *Appendix C*. The conclusions and open lines of investigation derived from this work is given in *Section 8*. Finally, a list of the used references is available at *Section 9*.

5 Theoretical Background

5.1 Propeller Theory Outline

As the chosen actuator for the application is a propeller, several considerations about the propeller theory will be given. First of all, basic concepts about the propeller as an aircraft and propulsion element and its geometry will be stated. Afterwards, a quantitative analysis which allows for the identification of the propeller efficiency $\eta_{profile}$ should be performed. The development stated by Von Mises [2] will be followed.

As mentioned in the introduction, the propeller may be regarded as "*strongly twisted wing*" [2], whose different cross-sections (see *Figure 1*) will not differ much from an actual wing. Another definition which would give an insight on its construction is the one given by Franchini and López [26], where the propeller arises as the composition of wing-like blades, formed by a variety of airfoils. These blades would interact with the surrounding flow generating an axial force propelling the aircraft in the direction of the propeller axis of symmetry. Such flow results as the combination of a freestream flow (with velocity equal to the aircraft airspeed) and the rotation of the propeller around its axis, thus resulting in a relatively complex velocity field, whose magnitude is thereby dependant on the radial position of the propeller (see *Equation 1*).

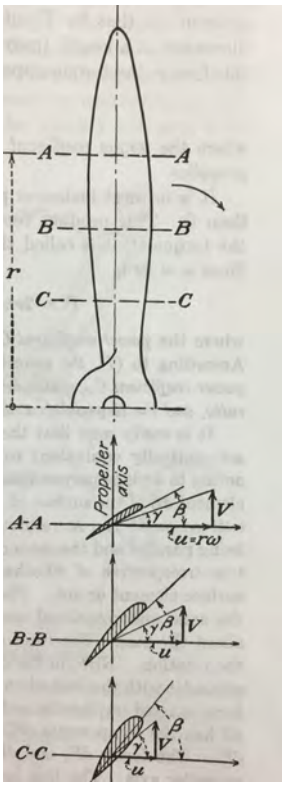

Figura 1: Propeller Cross Sections [2]

$$\mathbf{V} = V_\infty \mathbf{i} + \omega r \mathbf{j} \tag{1}$$

Where $\mathbf{i}$ is the unity vector in the direction of the propeller axis and $\mathbf{j}$ the unity vector. $\mathbf{V}$ would be the velocity field around the propeller, and ω the angular velocity (radians per second). Two angles take importance in the analysis of the propeller. One of them is the *advance angle*, and accounts for the angle between the velocity vector at each radial position and the plane of rotation (see *Equation2*). The second one is the *pitch angle*, and corresponds at the angle between the plane of rotation and an arbitrary reference line at each cross section. The pitch angle distribution is also known as the propeller *blade setting* Due to the fact that the blades construction is based in existing airfoils, usually the chord is chosen. However, when performing the aerodynamic analysis of the propeller, it is sometimes more convenient to choose another reference line, such as the zero-lift line for a given cross section.

$$\tan\gamma = \frac{V_\infty}{\omega r} \tag{2}$$

If the pitch angle distribution is known, as well as the value of the advance angle at one point (usually the blade tip is taken), it is possible to find the angle of attack

distribution alongside the blade. Through the advance angle at the blade tip, the dimensionless coefficient *advance ratio* of the propeller is obtained (J, see *Equation 3*). This coefficient would enable for both the comparison of geometrically similar propellers, as well as building the propeller performance charts.

$$J = \frac{V_\infty}{nd} \tag{3}$$

Where n is the angular velocity of the propeller (revolutions per second) and d stands for the propeller diameter.

The geometry of the propeller (also called airscrew) is closely related to the family of analytic surfaces called *helical surfaces*. Such surfaces are formed by the helical motion of a generic element (or generatrix) L, which is a motion composed of two different movements: a rotation about an axis of revolution (which will be called the *helical axis*) and a translation alongside such axis. A special case arises when the element L is a point A. Thus, the helical motion of A receives the term *helix*. The general helical surface with generatrix L in the form $z = f(r)$ with helical axis Oz may be expressed by the following vector equation in Cartesian coordinates [27]:

$$\mathbf{r}(r, \phi) = r\cos\phi\mathbf{i} + r\sin\phi\mathbf{j} + [f(r) + a\phi]\,\mathbf{z}$$

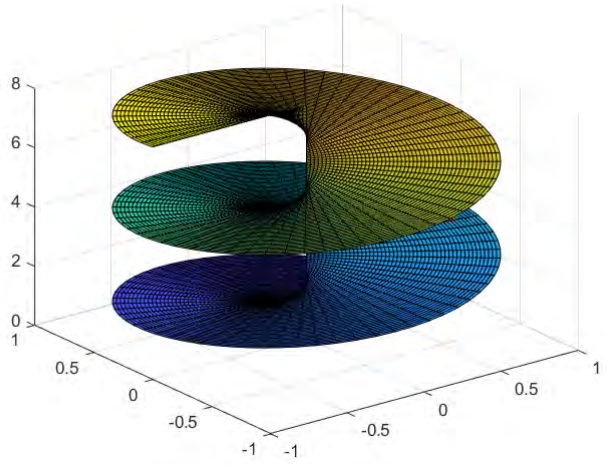

Figura 2: Ruled Helical Surface Example

Where r is the shortest distance between a point of the helical surface and the axis of symmetry, ϕ is the angle between the projection of a surface point in the xy plane with the x axis and a is a parameter representing the distance travelled along the helical axis for one complete revolution. Such parameter is called the *pitch* of the helical surface and in the aeronautical industry is often denoted by the letter p. The vectors $\mathbf{i}$, $\mathbf{j}$ and $\mathbf{k}$ are just the orthogonal unitary base for the Cartesian coordinate system.

Regarding the propeller case, the helical surface lies upon the category of ruled helical surfaces, defined as the family of surfaces formed "*when a straight line or its part is subdued to a helical motion*" [27]. If a segment of a straight line normal to the helical axis is forced to perform a helical motion along the aforesaid axis, a helical surface with the line as generatrix will be created (see *Figure 2*). A narrow strip of such surface is considered. For such strip, each of the points composing the generatrix perform helices. If each point helix under the narrow strip is considered as a straight line, the obtained group of lines could form the basis for a propeller shape (for instance, said lines could be the chord of each propeller cross section). An example for such case is considered in *Figure 3*, where the generatrix (red line) at two positions is considered, and the helix of three points has been shown (blue lines). For the sake of clarity, the helix trajectories are projected on the xy and yz planes. The black line represents the helical axis, located at the Oz axis.

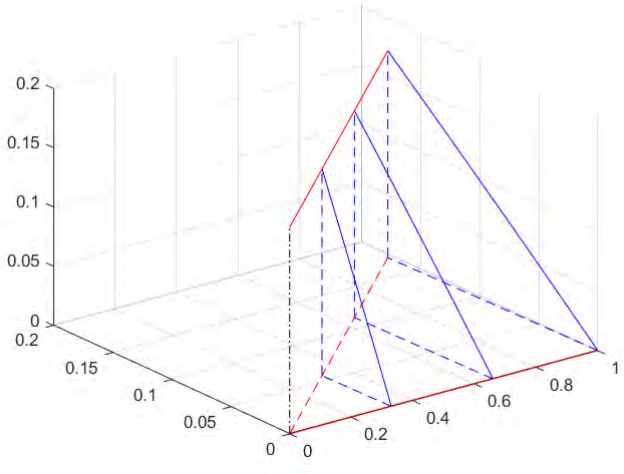

Figura 3: Helical Surface Strip

Thereby, it is possible to derive an expression for the pitch angle of a given cross section from the presented geometric considerations:

$$\tan\beta = \frac{p}{2\pi r} \tag{4}$$

This relation enables us to compute the angle of attack (α) at each cross section, or the angle of attack relative to the zero lift reference line (α'), by comparing the pitch angle distributions with the advance angle distribution:

$$\alpha = \beta - \gamma \tag{5}$$

$$\alpha' = \beta' - \gamma \tag{6}$$

Assuming the propeller as a composition of independent and known geometry airfoils, with a given blade setting and operating at certain advance ratio, it is possible to approximate the thrust and power given received from it, as well as its efficiency. If each cross section yields a specific thrust value, as well as opposing the propeller rotation with a given momentum, the thrust (see *Equation 7*) developed

by one propeller blade and the power(see *Equation 8*) needed to maintain its rotation at a certain angular velocity may be obtained from the addition of all the cross section contributions [26].

$$T = \int_0^R T(r)\, dr \tag{7}$$

$$P = \int_0^R \omega r Q(r)\, dr \tag{8}$$

Where $T(r)$ and $Q(r)$ are respectively the thrust distribution along the propeller blade and the moment contribution with the propeller axis as the reference line. Thus, evaluating the thrust and power at each cross section would enable us for the propeller performance evaluation. For such purpose, the analysis provided by the *Blade Element Theory* (BET) will be followed.

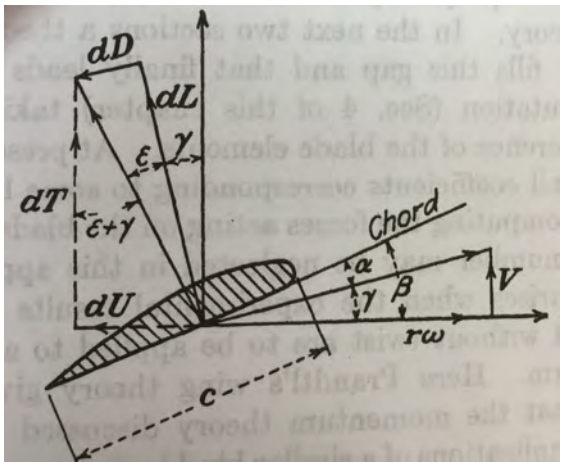

Figura 4: BET Forces Analysis [2]

The analysis starts with a generic cross section of the blade (see *Figure 4*), located at distance r from the propeller axis and pitch angle β with known operating conditions given by the angular velocity ω and the aircraft velocity V in the direction of the propeller axis. The shape of the cross section is of a known geometry airfoil of chord c, for which its aerodynamic coefficients (C_L and C_D) are assumed to be also known over a wide enough range of angles of attack. Taking the thrust as the force acting in the direction of the propeller axis and U the force acting perpendicular to it, the forces contribution from this cross section would be:

$$dT = dL\cos\gamma - dD\sin\gamma \tag{9}$$

$$dU = dL\sin\gamma + dD\cos\gamma \tag{10}$$

From *Equation 5* the angle of attack at the operating conditions is obtained, as the advance angle and blade setting are available data. Therefore, the aerodynamic forces acting at the cross section are fully identified by assigning the cross section a thickness dr.

$$dL = C_L \frac{1}{2} \rho V_{effective}^2 c\, dr = C_L \frac{\rho}{2} n^2 d^2 \left[J^2 + \left(\frac{2\pi r}{d} \right)^2 \right] c\, dr \tag{11}$$

$$dD = C_D \frac{1}{2} \rho V_{effective}^2 c\, dr = C_D \frac{\rho}{2} n^2 d^2 \left[J^2 + \left(\frac{2\pi r}{d} \right)^2 \right] c\, dr \tag{12}$$

Where J is the advance ratio, d the propeller diameter and n the angular velocity in revolutions per second. The reference surface from which the aerodynamic forces will be computed is obtained from assuming as an approximation the area of an infinitely thin airfoil, which in the current scenario will take the value:

$$dS = c\, db = c\, dr \tag{13}$$

From *Equations 11 and 12* it is possible to obtain an analytic expression for obtaining the propeller thrust, where m is the number of blades in the propeller.

$$T = m \frac{\rho}{2} n^2 d^2 \int_0^{d/2} \left[J^2 + \left(\frac{2\pi r}{d} \right)^2 \right] (C_L \cos\gamma - C_D \sin\gamma) c\, dr \tag{14}$$

However, even with the direct proportionality relation between the propeller number of blades and the developed thrust, it is not possible to keep increasing the number of blades in order to gain a higher thrust due to mutual interference between the blades. There has been numerous works in the literature working to assess the phenomena with a high degree of accuracy, especially in the field of ocean engineering and turbomachinery through the study of cascade airfoils, i.e. [28] and [29]. However, such detail level is assumed contribute in a negligible manner with the expected results, as the chosen propeller will have only two blades, and thereby left out of the scope of this work.

Recalling *Equation 44*, and by applying the definition of the moment of a force with respect to a given axis, it is possible to obtain the resultant torque actuating on the propeller shaft and opposing the propeller motion. Thus, the associated power which should be provided to the propeller to maintain its rotation speed is given by *Equation 17*

$$Q = m \int r\, dU \tag{15}$$

$$P = \omega Q = 2\pi n m \int r\, dU \tag{16}$$

$$P = \pi n m \rho n^2 d^2 \int_0^{d/2} \left[J^2 + \left(\frac{2\pi r}{d} \right)^2 \right] (C_L \sin\gamma + C_D \cos\gamma) r c\, dr \tag{17}$$

Finally, the propeller efficiency needed for the power balance equation may be computed from the obtained thrust and power expressions. The comparison will be made between the power provided by the propeller and available for the aircraft

propulsion (TV) and the needed power that may be transmitted to the propeller for it to maintain its rotation (P).

$$\eta = \frac{TV}{P} \tag{18}$$

Although the presented equations close the propeller efficiency problem with a relatively high degree of accuracy, it is possible to simplify the problem taking into account experimental measures will be carried out. First of all, a dimensional analysis on the propeller performance parameters (T and P) will be executed, yielding the following *thrust coefficient* and *power coefficient* as functions of the propeller diameter (d), rotation speed (n) and working fluid density (ρ).

$$C_T = \frac{T}{\rho n^2 d^4} \tag{19}$$

$$C_P = \frac{P}{\rho n^3 d^5} \tag{20}$$

The evolution of these propeller performance coefficients with the advance ratio at any operating conditions yields the propeller characteristic charts, which summarise its performance and serve as the basis for the comparison of several propellers, in order to choose the most appropriate one for a given mission. An example of such charts is given for a propeller with similar characteristics ($9'' \times 4.7''$) to the one used in this experiment ($9'' \times 5''$).

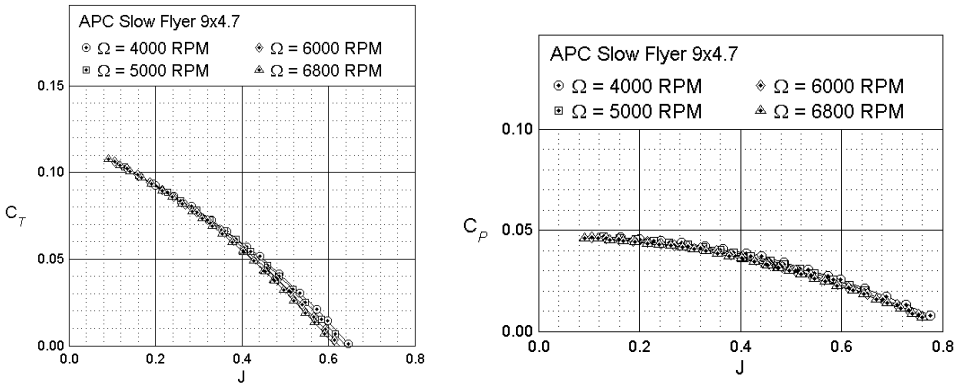

(a) C_T Example Chart (b) C_P Example Chart

Figura 5: Propeller Performance Charts Example [30]

Making use of *Equations 19* and *20*, it is possible to simplify the efficiency relation to the following expression, which is the one which will be employed when computing the power terms in the power balance method:

$$\eta = \frac{C_T}{C_P} J \tag{21}$$

Therefore, before performing the experiment, the propeller characterisation (development of its power and thrust coefficients curves over its operating conditions range J) will be performed, in order to obtain its efficiency distribution.

5.2 Power Balance Method

As stated in the Introduction, physical models focusing on the acting forces have been the traditional approach when dealing when an engineering problem, especially in the aeronautical field. Once the force analysis was complete, the thermodynamic relations would be used to relate the state variables, thereby closing the problem. However, this approach remains insufficient when analyzing revolutionary designs or concepts which involves for instance propulsive systems closely integrated in the airframe. As they do not ingest freestream flow, but rather a flow modified by the presence of the airframe, the definition of the thrust provided or each system net streamwise force becomes confusing. This is due to the impossibility of clearly defining the boundaries of one system from the other the majority of times.

Searching for a solution to this issue, past models which were discarded in benefit of such traditional approach have been rescued, and are being redeveloped to attend the current engineering needs. One of the most complete approaches is the one involving the exergy concept. Several definitions may be encountered in the literature. One of the most general ones is the one given by D. S. Scott [16], who defines exergy as "*energy that's out of equilibrium with its environment*".Thus exergy could be classified upon three kinds: mechanical (often due to differences in pressure), thermal (always due to differences in temperature) and chemical (including electrochemical reactions, such as batteries). However, the more developed explanation given by Arntz [15] becomes more illustrative for the current application: "*Exergy is a thermodynamic property describing the maximum theoretical work that can be obtained from a substance in taking it from a given temperature and pressure/velocity to a state of thermal and mechanical equilibrium with its environment [...] being here taken as the atmosphere at the altitude of flight*". It is remarkable the fact that this definition leaves out the chemical exergy which may be produced in the system, as it is assumed that no chemical reactions take place outside the propulsion system. The energy which is not convertible to work, and thus will be associated to irreversible losses within the system (associated with entropy increase) is called anergy. Thus, the following distinction may be stated:

$$Energy = Exergy + Anergy$$

On the other hand, for the current application thermal exchanges will be assumed not to greatly modify the experiment, and thereby negligible. Thus, as the only exergy applicable is the mechanical one (directly related with velocity and pressure fields), Drela [14] power balance model will be worked upon, as well as taking into account the theoretical development by Lv et al. [18] including wake and boundary layer ingesting actuators. First of all, Drelas's work will be presented. Later on, modifications added by Lv et al. will be introduced. Finally, the resulting set of equations will adjusted to the application concerned.

The power balance model is based on a mechanical energy analysis. It starts with the time-averaged momentum equation in divergence form:

$$\boldsymbol{\nabla} \cdot (\rho \mathbf{V}\mathbf{V}) = - \bigtriangledown p + \boldsymbol{\nabla} \cdot \overline{\overline{\tau}} \tag{22}$$

Where $\mathbf{V}$ is the time-averaged velocity vector, p the time-averaged pressure field and $\overline{\overline{\tau}}$ the time-averaged viscous stress tensor. By applying to *Equation 22* the dot product with the velocity and using the following vector identities:

$$\boldsymbol{\nabla} \cdot a\mathbf{B} = \bigtriangledown a \cdot \mathbf{B} + a\boldsymbol{\nabla} \cdot \mathbf{B}$$

$$\boldsymbol{\nabla} \cdot (\overline{\overline{c}} \cdot \mathbf{B}) = (\boldsymbol{\nabla} \cdot \overline{\overline{c}}) \cdot \mathbf{B} + (\overline{\overline{c}} \cdot \bigtriangledown) \cdot \mathbf{B}$$

The following equation is obtained:

$$\boldsymbol{\nabla} \cdot \left(\frac{1}{2} \rho \mathbf{V} V^2 \right) = -\boldsymbol{\nabla} \cdot p\mathbf{V} + p \bigtriangledown \cdot \mathbf{V} + \boldsymbol{\nabla} \cdot \overline{\overline{\tau}} \cdot \mathbf{V} - (\overline{\overline{\tau}} \cdot \bigtriangledown) \cdot \mathbf{V} \tag{23}$$

Integrating *Equation 23* over the whole control volume, and applying the Gauss or divergence Theorem ("*if the flux of a vector field* $\mathbf{f}$ *is zero through every closed surface containing a given point, then* $\boldsymbol{\nabla} \cdot f = 0$ *at that point*" [23]), yields the integral mechanical power balance equation, whose terms will be explained below.

$$P_s + P_V + P_k = \dot{\varepsilon} + \Phi \tag{24}$$

The right side terms account for the mechanical energy sources, with three possible contributions:

$\mathbf{P_s}$ is the propulsor shaft power, and accounts for the integrated force times velocity over all the moving body surfaces. This power would include, if decided, boundary-layer control systems, flapping wings and exposed turbomachinery bladings. Its derived formula in integral form is as follows:

$$P_s = \oiint [-(p - p_\infty)\mathbf{n} + \tau] \cdot \mathbf{V} \, d\mathcal{S}_\mathcal{B} \tag{25}$$

$\mathbf{P_V}$ is defined as the net pressure volume power, which is the mechanical power given by the expansion of the fluid against a given reference pressure. For aeronautic applications, such pressure would be the atmospheric pressure (p_∞). Such power is provided by the following formula:

$$P_V = \iiint (p - p_\infty) \boldsymbol{\nabla} \cdot \mathbf{V} \, d\mathcal{V} \tag{26}$$

$\mathbf{P_K}$ is the net propulsor mechanical energy flow rate into the control volume, which accounts for moving sources not included into the body surfaces. Such term is given by the following relation:

$$P_K = \oiint - \left[(p - p_\infty) + \frac{1}{2} \rho (V^2 - V_\infty^2) \right] \mathbf{V} \cdot \vec{n} \, d\mathcal{S}_\mathcal{B} \tag{27}$$

The right side terms in *Equation 24* account for either the power losses inside or leaving the control volume.

Φ includes the viscous dissipation inside the control volume which measures how fast the fluid kinetic energy is transformed into thermal energy. This term is in direct relation to the viscous stress tensor, as shown below:

$$\Phi = \iiint (\overline{\overline{\tau}} \cdot \bigtriangledown) \cdot \mathbf{V} \, d\mathcal{V} \tag{28}$$

On the other hand, $\dot{\varepsilon}$ is the control volume mechanical energy outflow rate, and may be fragmented into five energy (see *Equation 29*) rate contributions: one of them reversible and the four others associated to irreversible losses. The four irreversible terms are evaluated at the outlet plane of the control volume.

$$\dot{\varepsilon} = W\dot{h} + \dot{E}_a + \dot{E}_v + \dot{E}_p + \dot{E}_w \tag{29}$$

$W\dot{h}$ states the potential energy rate, and is the only reversible component included in *Equation 29*. Such term indicates the needed power to increase the potential energy of the aircraft, and would thereby become an energy source whenever the aircraft loses height, being W the aircraft weight, $\dot{h}$ the climb rate and γ the climb angle.

$$W\dot{h} = -F_x V_\infty = W V_\infty \sin\gamma \tag{30}$$

$\dot{E}_a$ includes the wake streamwise kinetic energy deposition rate, where u is the streamwise component of the perturbation or induced velocity vector (parallel to the freestream velocity). This term will always be positive assuming no recirculation happens outside the control volume, and thus no fluid flows back into it. Such term is evaluated in the following way:

$$\dot{E}_a = \iint \frac{1}{2}\rho u^2 \left(V_\infty + u\right) \, d\mathcal{S}_o \tag{31}$$

$\dot{E}_v$ represents the wake transverse kinetic energy deposition rate. In includes both directions not represented by the streamwise direction (v and w respectively). Assuming the streamwise induced velocity is much neglible when compared to the freestream, this term accounts for the induced drag (D_i) of the aircraft.

$$\dot{E}_v = \iint \frac{1}{2}\rho \left(v^2 + w^2\right) \left(V_\infty + u\right) \, d\mathcal{S}_o \tag{32}$$

$\dot{E}_p$ identifies the wake pressure defect work rate. In other words, it represents the pressure work performed by the fluid leaving the control volume as a consequence of a different pressure with respect to the reference one.

$$\dot{E}_p = \iint \frac{1}{2}\rho \left(p - p_\infty\right) u \, d\mathcal{S}_o \tag{33}$$

The final term (**$\dot{E}_w$**) performs the same operations as *Equations 10-12* but integrating along the side cylinders walls of the control volume. However, it has been stated that this term decreases as $1/r^4$ for subsonic 3-D walls [14]. Therefore, with sufficiently enough distant side walls, this term would become negligible.

Taking all the terms into account, the change in power flight for a tightly system integrated aircraft could be expressed by the addition of all the power sources and sinks plus the addition of all the viscous dissipation terms:

$$\Delta P = \sum \Delta \dot{E} + \sum \Delta \Phi \tag{34}$$

The work developed by Lv et al. [18] main modification to the previously presented power balance method is the definition of an internal interface (from now on inlet plane) at the beginning of the selected control volume to asses the energy rate inflow. For instance, for the case of general actuator with a non-uniform inflow (see *Figure 6*) the power balance would be built in the following way. The control volume chosen is a cylinder whose side walls are placed sufficiently far away such that the pressure at the walls becomes the reference pressure, and the inlet plane is placed sufficiently upstream so that the flow has freestream pressure value over all the inlet plane.

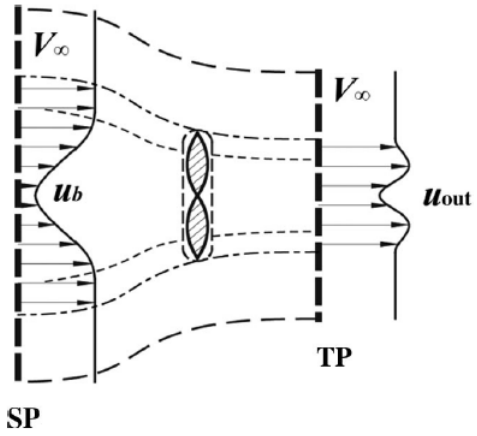

Figura 6: General Actuator Control Volume [18]

Thus, following the approach stated by *Equation 34*, the power balance for this case would imply, assuming that the flight power remains constant, as the "aircraft" would neither decrease nor increase its kinetic or potential energy, that the power sources balances the power sinks as well as the viscous dissipation.

$$\dot{E}_{in} = \dot{E}_{out} + \Phi \tag{35}$$

The power sources ($\dot{E}_{in}$) right side of the equation is expanded into the following way, by applying the method exposed before.

$$\dot{E}_{in} = \dot{E}_{a,in} + \dot{E}_{v,in} + \dot{E}_{p,in} + \dot{E}_{w,in} + P_{prop} \tag{36}$$

Introducing the actual conditions for the selected case, the only power sources would be the power supplied into the control volume by the propeller and the axial kinetic energy given by the inflow (KE_{in}, associated with $\mathbf{u}_b$). It has been assumed that such inflow is steady, and with magnitude variation as shown in *Figure 6*. Its analytic relations are depicted below.

$$\dot{E}_{a,in} = \iint \frac{1}{2} \rho u_b (u_b - V_\infty)^2 \, d\mathcal{S}_{inlet}$$

$$P_{prop} = Q\omega$$

Where u_b is the velocity field magnitude value normal to the inlet plane, V_∞ is the freestream velocity, ρ the fluid density, Q the actuator developed torque and ω the actuator rotational speed in radians per second.

On the other hand, an analogous procedure is applied to the power sinks ($\dot{E}_{out}$), not taking into account the viscous dissipation, which will be discussed later on.

$$\dot{E}_{out} = \dot{E}_{a,out} + \dot{E}_{v,out} + \dot{E}_{p,out} + \dot{E}_{w,out} + TV_\infty$$

As discussed before, $\dot{E}_{w,out}$ becomes negligible for sufficiently distant side walls. Therefore, the power sinks relation reduces to:

$$\dot{E}_{out} = \dot{E}_{a,out} + \dot{E}_{v,out} + \dot{E}_{p,out} + TV_\infty \tag{37}$$

With each term expressed by the following relations:

$$\dot{E}_{a,out} = \iint_{outlet} \frac{1}{2} \rho u_{out} (u_{out} - V_\infty)^2 \, d\mathcal{S}_{outlet}$$

$$\dot{E}_{v,out} = \iint \frac{1}{2} \rho \left(v_{out}^2 + w_{out}^2 \right) \left(V_\infty + u_{out} \right) \, d\mathcal{S}_{outlet}$$

$$\dot{E}_{p,out} = \iint (p_{out} - p_\infty) u_{out} \, d\mathcal{S}_{outlet}$$

Where u_{out}, v_{out} and w_{out} are the outlet velocity field components and p_{out} the pressure at the outlet plane. For low subsonic flows, a relation between the velocity magnitude and pressure values may be addressed by the Bernoulli theorem.

With regards to the viscous dissipation term (Φ), it is a complex term highly dependant on the problem geometry and the operating conditions. Its full formulation requires that the velocity field and fluid viscous tensors are available (see *Equation 28*), though a simplified approach is developed by Lv et al. [19], in which only the u and w dominant terms contributions are included (see *Equation 38*). This term will be looked for and investigated in the downstream wake of the control volume. However, its contribution due to viscous stresses on the control volume surfaces is assumed to be negligible of the order of less than 0.01% of the actuator developed power [25]. Thus, the vast majority of viscous dissipation will take place in the wake and bodies boundary layer.

$$\Phi \approx \iiint_{CV} \left(\left[\mu \left(\frac{\partial u}{\partial y} \right)^2 - \rho u' v' \frac{\partial u}{\partial y} \right] + \left[\mu \left(\frac{\partial w}{\partial y} \right)^2 - \rho u' v' \frac{\partial w}{\partial y} \right] \right) \, d\mathcal{V} \tag{38}$$

Another application which would prove useful to be analysed by the power balance method would be a bluff body immersed in a freestream flow, The control

volume chosen (see *Figure 7*) is again of cylindrical shape encompassing the body. Homogeneous, steady flow is considered at the inlet plane, while the side cylinder walls are placed far enough to achieve ambient conditions at the boundaries.

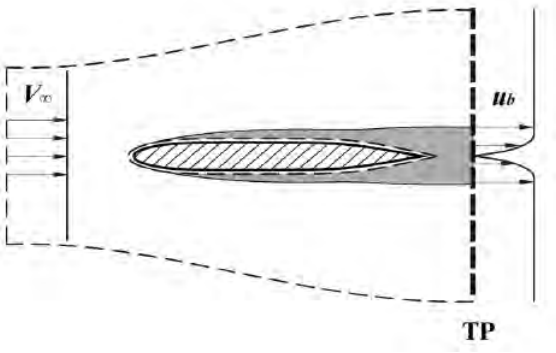

Figura 7: Bluff Body Control Volume [18]

The power balance relation for this case becomes:

$$\dot{E}_{in} = \dot{E}_{out} + \Phi \tag{39}$$

With the only power source being the incoming kinetic energy from the freestream flow:

$$\dot{E}_{in} = \dot{E}_{a,in} = \iint \frac{1}{2}\rho u_b(u_b - V_\infty)^2 \, d\mathcal{S}_{inlet}$$

As may be observed, assuming the freestream flow is homogeneous over all of the inlet plane, this term will vanish. On the other and, the power sinks accounts for the body wake leaving the control volume (both its pressure and velocity defects):

$$\dot{E}_{out} = \dot{E}_{a,out} + \dot{E}_{p,out} = \iint \frac{1}{2}\rho u_{out}(u_{out} - V_\infty)^2 \, d\mathcal{S}_{outlet} + \iint \frac{1}{2}\rho(p_{out} - p_\infty)u_{out} \, d\mathcal{S}_{outlet}$$

The viscous dissipation term taking part inside the control volume (Φ) have two main contributions. On one hand, the viscous dissipation taking place in the boundary layer of the bluff body, as well as the pressure based drag related energy dissipation. On the other hand, the energy dissipation in the turbulent region after the bluff body (shaded region in *Figure 7*). These two terms should be investigated if a fully description of the energy dissipation mechanisms is required. Nevertheless, as stated by Drela [14], if the outlet plane is placed sufficiently downstream such that the velocity profile has recovered to the freestream condition (in other words, no wake energy outflow remains), the viscous dissipation would amount to the body drag power.

$$\Phi_{total} = DV_\infty \tag{40}$$

This equation may be explained from another point of view which would prove useful when analyzing the control volume considered for a general integrated system (airframe and propulsion). As the bluff body is theoretically supposed to be

travelling at an airspeed equal to that of the freestream flow (though for the derived method the reference frame is centered on the body), some power must be supported to the body in order to maintain that speed. Thus, such required power would amount to the force needed to sustain that motion (constant speed V_∞). In order to have a constant velocity motion, body acceleration must be zero, which would imply equilibrium of forces for the bluff body. Thus, the force applied to the body should be equal to its drag, with the power applied to the body modelled as DV_∞. Such power would at the end become dissipated by the viscous dissipation term in order for the mechanical balance to hold. To sum up, the drag related power has become now a power source, while viscous dissipation accounts for the only power sink.

Finally, the case considered here would consist of the combination of the two already explained cases, with some particularities. Distinction between WI or BLI regimes rely on whether the fluid pressure has regained the ambient value after encountering the bluff body ($p = p_\infty$, for the WI case) or not ($p \neq p_\infty$). In case the problem was modeled as a simple superposition this theoretical aspect would have some importance, as the input power terms for the actuator control volume would consist on the bluff body outflow (thus, its kinetic energy and pressure wake defect). However, one of the advantages the power balance method holds is the possibility of fusing both the bluff body and the actuator control volumes into the same one, regarding the elements the process between them as intermediate transient ones.

Therefore, the control volume chosen would be of cylindrical shape, encompassing both the sphere (chosen bluff body thanks to the amount of literature describing flows past it along a variety of circumstances, with a diameter D) and the propeller (actuator, with diameter d). The cylinder walls are chosen at a distance of $1.5D$ from the sphere center, and pressure is assumed to have recovered to the ambient value (p_∞). At the inlet plane, the velocity profile is assumed to be steady and homogeneous (valued V_∞, with pressure p_∞), centered at the sphere-propeller axis. Thus, the power balance for this scenario would again be:

$$\dot{E}_{in} = \dot{E}_{out} + \Phi$$

The power sources ($\dot{E}_{in}$) at the left side of the equation would come as a combination from the two aforementioned cases. First of all, the inflow wake kinetic energy from the freestream flow ($\dot{E}_{a,in}$), which as discussed before may be assumed zero if homogeneous conditions apply at the inlet plane. Nevertheless, this term will be conserved in the following equations for the sake of generality. Next, as earlier stated, the power needed to maintain the body at the given freestream velocity is considered as a power source as well (DV_∞). The last energy source would come from the power supplied by the propeller to the control volume (P_{prop}).

$$\dot{E}_{in} = \dot{E}_{in,a} + DV_\infty + P_{prop} \tag{41}$$

On the other hand, the main power sinks ($\dot{E}_{out}$) for the control volume may be obtained again as a combination from the bluff body and freestream actuator

cases. First of all, the thrust related power developed by the actuator (TV_∞). Afterwards, the wake energy leaving the control volume, both in its streamwise and transverse velocity components, as well as the pressure energy term ($\dot{E}_w$).

$$\dot{E}_{out} = TV_\infty + \dot{E}_w \tag{42}$$

Each term derivation is stated in the following lines:

$$\dot{E}_{in,a} = \iint \frac{1}{2} u_b (u_b - V_\infty)^2 \, d\mathcal{S}_{inlet} = 0 \tag{43}$$

$$P_{prop} = Q\omega \tag{44}$$

$$\dot{E}_{w,out} = \dot{E}_{w,a} + \dot{E}_{w,v} + \dot{E}_{w,p} \tag{45}$$

$$\dot{E}_{w,a} = \iint \frac{1}{2} \rho u_{out} (u_{out} - V_\infty)^2 \, d\mathcal{S}_{outlet}$$

$$\dot{E}_{w,v} = \iint \frac{1}{2} \rho (v_{out}^2 + w_{out}^2)(u_{out} + V_\infty) \, d\mathcal{S}_{outlet}$$

$$\dot{E}_{w,p} = \iint (p_{out} - p_{out}) u_{out} \, d\mathcal{S}_{outlet}$$

For the sake of simplicity, the drag and thrust related powers will be fused into a new term, containing the net force (N) power contribution. Therefore, for the equilibrium case ($N = 0$) this term will vanish from the equation. The power balance for the general case of a body + actuator system would then read:

$$\dot{E}_{in,a} + P_{prop} = NV_\infty + \dot{E}_w + \Phi \tag{46}$$

Regarding the viscous dissipation (Φ), it may be separated into its composing terms. However, as it is the term which will be investigated upon, it will remain unmodified, for the sole exception that it is possible to approximate the viscous dissipation taking place in the vicinity of the propeller. Thus, the viscous dissipation decomposition would be:

$$\Phi = \Phi' + \Phi_{prop}$$

Where Φ_{prop} is the viscous dissipation taking place at the propeller profile boundary layers and Φ' the viscous dissipation in the rest of the control volume (sphere and after propeller wakes). The first could be modelled as suggested by Drela [14] by the following relation:

$$\Phi_{prop} = P_{prop}(1 - \eta_{profile})$$

Where $\eta_{profile}$ is the overall profile efficiency coefficient. Such term calculation will be developed in the following section. Thus, if introduced into *Equation 46*, it becomes:

$$\dot{E}_{in,a} + \eta_{profile} P_{prop} = NV_\infty + \dot{E}_w + \Phi' \tag{47}$$

6 Experimental Set Up

In order to carry out the experiments, a convenient set up needs to be designed and built for the both possible scenarios: University open and closed loop wind tunnel facilities. First of all, the set up for the open loop wind tunnel will be described in *Subsection 6.1*. This includes the description and design process for all the structural components. The design process, including part design, assembly routine and blueprints creation was carried out with the academic version of the *Solid Edge* software. The blueprints for the manufactured pieces in the University workshop are given in *Appendix B*. Afterwards, the implementation of the experiment in the closed loop tunnel will be given in *Subsection 6.2*. Next, the electronic devices involved in the measurements will be listed and explained in *Subsection 5*, with a table summarising their Supplier and Cost is available in *Appendix A*. Mechanical components employed in the set up building process are also accounted for. It is important to remark that, although the set up was at first built and preliminary test carried out in the open loop wind tunnel, final data measurements were carried out in the closed loop wind tunnel. Afterwards, closed wind tunnel corrections which were taken into account are derived and explained in *Subsection 6.4*. In addition, the error analysis for the obtained results is shown in *Subsection 6.5*. To close the set up design, its regulatory framework and budget is detailed in *Subsection 6.6*.

6.1 Open Wind Tunnel Set Up Design

The experiment will first be carried in the open wind tunnel facilities of the UC3M (see *Figures 8a and 8b*). The wind tunnel is formed by a low pressure compressor (*MundoFan BP MC 9/9 6P*) to provide the required airflow, a potentiometer (*MundoFan RV-MU 5A*) to control the airflow, and a convergent nozzle at the compressor outlet, with a squared (200x200 mm) cross section exit plane. The provided flow will be assumed to be homogeneous. The wind tunnel is located in a 1 meter height table, with a distance of 100 mm between the table and the lower edge of the nozzle exit section.

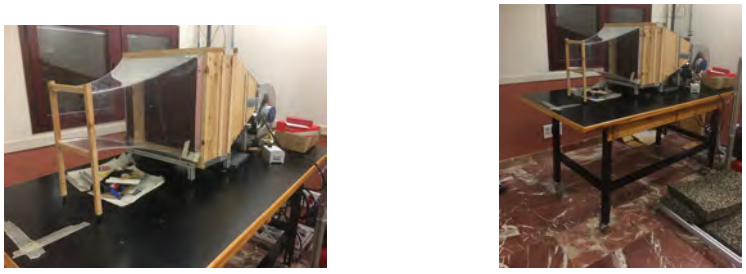

(a) Open Wind Tunnel Detail (b) Open Wind Tunnel

Figura 8: Open Wind Tunnel Facility

Thereby, the required structure for the experiment would need to sustain the propulsion unit (propeller and motor), the bluff body (sphere) and the associated electronics needed for both controlling the propeller and taking the appropriate measurements (sphere drag, propeller thrust, torque and rotational velocity). For

such purpose, the propeller and sphere should lie on a coincident axis passing through the center of the squared nozzle exit (at 1350 mm from the floor).

In order to build the structure, slotted aluminium profiles (with 30x30 mm cross section) will be employed, connected between themselves with T-nuts and 90º connectors. Conceptual design of the structure is shown in *Figure 9a*. The conceptual design was conformed of a one leg floor support with four foots, a horizontal slotted profile upon which will be mounted the propulsive unit and sphere, as well as the electronics, and the connection to the table, which would be conformed by a two feet support relying on the structure own weight. Details on the propulsion unit and sphere supports were left aside for the next design stage.

(a) Open Wind Tunnel Conceptual Design (b) Open Wind Tunnel Design

Figura 9: Conceptual Design

As may be observed in *Figure 9b*, some minor changes were applied to the structure. First of all, the original four-legged foot was replaced with a mounted leg (see *Figure 10*), as the irregularities in the floor level resulted in structure instabilities. On the other hand, the two aluminium slots which were initially designed to serve as the structure support on the table were substituted by a sandwich-like sub-assembly (see *Figure 11*). Such sub-assembly was built by perforating twice the main slotted profile and another shorter profile. Afterwards, two M6 threaded bars would be introduced and secured by washers and nuts. Thereby, the sub-assembly will allow for a strong and customised grip to the table, ensuring the structure would stay in place and absorb to some degree the motor vibrations. Further stable options were considered, such as perforating the table in order to ensure a more even grip load distribution, though were discarded for the sake of simplicity.

Figura 10: Structure Floor Support Detail

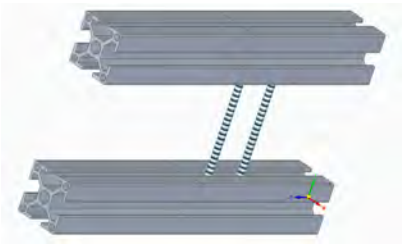

(a) Sandwich Connection Concept

(b) Sandwich Connection

Figura 11: Sandwich Connection

Finally, the main structure will be displaced to the lateral of the nozzle exit for two main reasons. First of all, to replicate the conditions at which the experiment will be carried in the closed section wind tunnel. Secondly, to eliminate potential structure interference in the incoming airflow. Therefore, the final supporting structure would require the propulsion unit and sphere to be displaced from itself 200 mm in the lateral direction and 350 mm in the upwards one.

In order to support the propulsion unit and sphere, two sub-assemblies were designed and produced. Regarding the sphere sub-assembly, it should allow for the sphere to lie at the center of the nozzle exit cross-section, as well as have integrated within it a mean of measuring the body drag. Such measurement will be performed by means of a 5kg load cell (blue colour). The sub-assembly design is shown in *Figure 12*. It is composed of a plate connected to the aluminium profile, the load cell, a 90º angle connector and a M6 threaded bar which will hold the sphere in place.

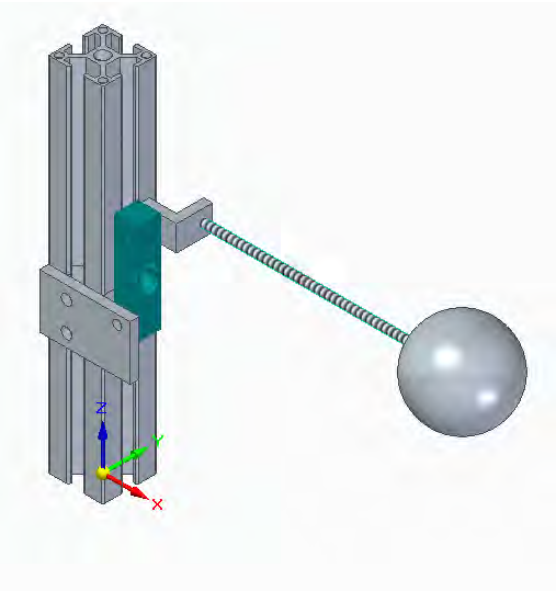

Figura 12: Sphere Support Conceptual Design

Additionally, a fairing will be designed in order to cover the threaded bar and ensure a smooth flow over the bar and its connection with the sphere. The fairing will be based in the NACA 0040 airfoil (zero camber with 40% maximum thickness), which despite providing a relatively high thickness, will ensure enough material will be surrounding the bar to avoid fairing fracture. This could have been achieved with a thinner airfoil, though at the cost of a higher chord. Therefore, the final fairing would have a chord of 20 mm with a maximum thickness of 8 mm. The airfoil shape was derived from the 4-digits NACA series equation [31]:

$$y_t = 5t\left[0.2969\sqrt{x} - 0.1260x - 0.3516x^2 + 0.2843x^3 - 0.1015x^4\right] \tag{48}$$

Where y_t is the half thickness of the airfoil from the center line, x coordinate points along the centerline (ranging from zero to the chord value c) and t the maximum airfoil thickness. The last coefficient (-0.1015) has been replaced by the value -0.1036 to provide zero thickness value at the trailing edge. Though there are multiple ways to obtain this effect, this is the one which respects the original shape the most. In order to obtain the airfoil surface, a script in *MATLAB* was produced, assigning 600 points for a unitary chord value half airfoil (totalling 1200 points for the whole airfoil). Such points were afterwards exported to *MS Excel* and modified to yield the desired chord and format specified by *Solid Edge*. For this airfoil, the maximum thickness is found in the vicinity of 6 mm from the airfoil starting point ($x = 0$). At that point, a hole is designed of diameter 5.2 mm. Therefore, as both the fairing and sphere will be 3D printed, the threaded bar will erode the plastic material and induce a threaded hole. In order to ensure a smooth connection between the fairing and the sphere, a special connector between them was also designed. The fairing and whole assembly design are shown in *Figures 13a and 13b*.

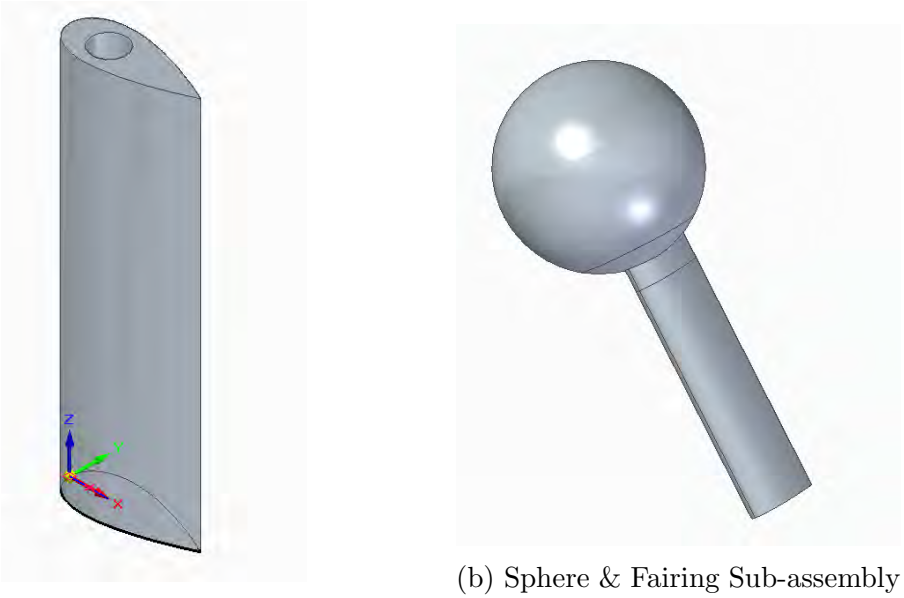

(a) Fairing

(b) Sphere & Fairing Sub-assembly Design

Figura 13: Fairing Design

Such pieces will be manufactured with the UC3M *Ultimaker 2+ Extended* 3D

printer. A 0.4 mm nozzle will be employed, which allows for a layer resolution of up to 20 μm and build speed of up to 16 mm^3/s. The printer XYZ resolution is 12.5/12.5/5 μm [33]. The material employed is PLA (polylactide) plastic filament, which is a biodegradable thermoplastic polyester with tensile strength of 110 MPa. The printing process is controlled the open-source software *Ultimaker Cura*.

Regarding the motor support, the structure holds a higher degree of complexity. Not only must it place the motor at the required spatial location and measure its thrust, but integrate additional load cells to measure the produced torque, whose values will be taken into account to measure the propellers developed power. The structure is composed of a plate connecting the slotted profile with the torque measuring load cells, which are connected by a T-shape piece to the thrust measuring load cell. As the torque may be defined as "*the moment of force caused by a couple that consists of a pair of forces with the same magnitude but in opposite directions*" [32]. As the load cells used to measure the torque are axial load cells (only measure the force applied through one axis of the application point), the torque yielded by the propeller may be expressed by the following relation:

$$Q = d(F_1 + F_2) \tag{49}$$

Where Q is the developed torque, d the distance of the forces to the axis lying of torque application point (shaft where the propeller is mounted) and F_1 and F_2 the measured forces by the load cells. Such distance, as obtained geometrically from the designed part (see *Figure 61*) is of 25 mm. The motor support structure design is shown in *Figure 14*, where the torque load cells are depicted in red and the thrust one in blue.

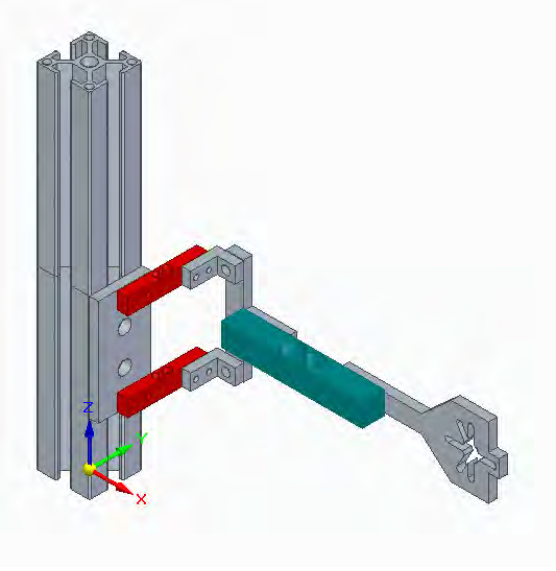

Figura 14: Motor Support Conceptual Design

Finally, the full structure may be observed in the following figures. This structure was employed to test all the set up components and ensuring that measurements were being taken correctly and as expected.

(a) Open Wind Tunnel Set Up *A* (b) Open Wind Tunnel Set Up *B*

Figura 15: Open Wind Tunnel Set Up

6.2 Closed Wind Tunnel Set Up Design

A similar set up is derived to work in the closed wind tunnel facility of the *UC3M*, which contains a 400x400x1500 mm test section. The advantage of carrying the experiment in such facility would be the exact characterisation of the flow going through the propeller and flow unit, as it is a closed system with precise information about the mass flow at the inlet plane (and, as a consequence applying the mass conservation theorem, through all the wind tunnel experimental section). However, the lack of space availability places a higher degree of complexity for the structure, as it should hold all the necessary equipment without introducing a severe flow blockage. In addition, flow and results in a closed loop wind tunnel needs to be corrected due to the different elements interacting with the flow fields. Employed corrections will be fully explained later on. The conceptual design for such set up is shown in *Figure 16*. As may be observed, the design is very similar to the one employed in the open wind tunnel facility. This fact results as a consequence of taking into account the closed tunnel complexities when designing the open tunnel set up, in order to make them as close in structure as possible. This will facilitate the comparison of results in future experiments.

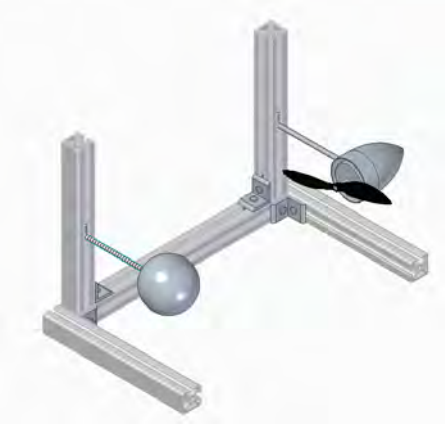

Figura 16: Closed Wind Tunnel Conceptual Design

The new requirements are to place the sphere and propulsion unit at the same streamwise axis, located at the center of the tunnel test cross section. In other words, the axis should lay at a 200 mm distance from each wall in order for it to be centred. Position in the streamwise axis is deemed irrelevant for the concerning application, and thus the structure is placed a little back from the centre position. The electronic components wires will be secured to the lateral walls of the wind tunnel in order to minimise potential blockage. The wires powering the devices and transmitting the necessary data to the computer (power, ground and USB wires for the RC Benchmark data acquisition board and USB wire for the Wheatstone bridge) will be passed through a pre-existing hole in the test section lateral wall. Once the set up has been installed, this hole will be covered by adhesive tape to minimise its effect on the airflow. Additionally, an extra slotted profile is threaded and connected (by a screw and T-nut) to the wooded lateral wall in order to further fix the structure and dissipate potential system vibrations. The complete set up is observable in *Figure 17*.

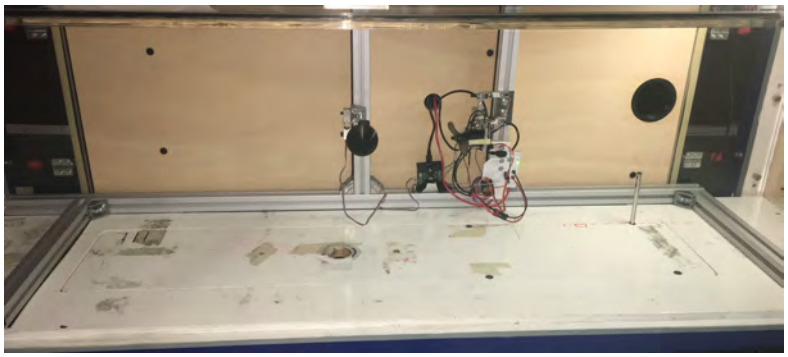

Figura 17: Closed Tunnel Set Up

Freestream velocity data at each experiment were obtained by means of a Pitot tube and a *HSCSRRN001NDAA5 Honeywell* pressure transducer, which takes into account the flow velocity at the beginning of the wind tunnel test section, the ambient pressure in the wind tunnel (which is assumed to be the same as the ambient pressure of the laboratory it is placed, measured by a commercial purpose weather

station with accuracy of 1 Pa) and the flow temperature. Such value is obtained by hot wire anemometry, located at the end of the test section, with accuracy of 0.01°C. The obtained data is measured by *LabVIEW* application, and later transcribed into a *.csv* file for its later analysis. In addition to the already described pieces (see *Subsection 6.1*), two extra pieces were manufactured to provide for a more stable support for the Wheatstone bridge (see *Figure 18a*) and the RPM magnetic device (see *Figure 18b*).

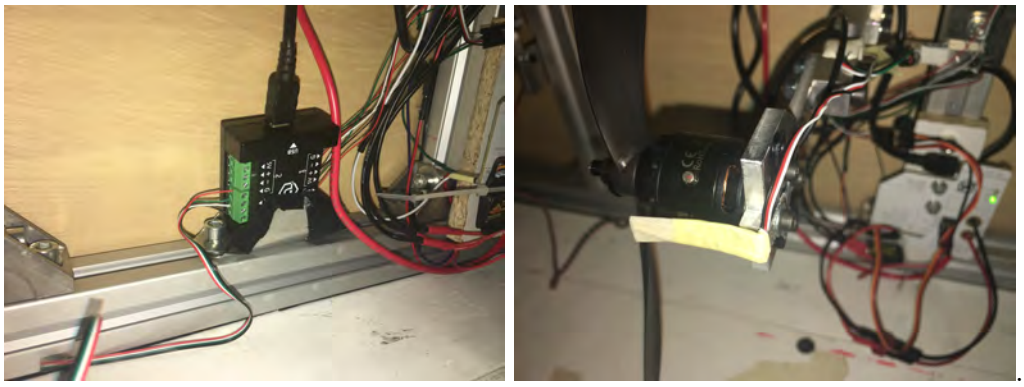

(a) Bridge Device Support (b) Magnetic Device Support

Figura 18: Additional Electronics Support Pieces

6.3 Electronic Components

?? Several electronic components will be involved in the experiment in order to accurately measure the key parameters stating the system performance. Regarding forces and torque measurements, beam load cells (5 kg and 780 g capacities) will be employed to efficiently assess their values. Such load cells will be connected to a Wheatstone bridge device in order to amplify the signal, and directly transmit the data to a PC by means of a built-in-purpose application. In order to obtain power the propeller, a Brushless DC (BLDC) motor will be employed connected to the RC Benchmark and controlled a 12 A Electronic Speed Controller (ESC). The motor will be coupled with a magnetic sensor to improve the accuracy of the angular velocity measurements. The Benchmark will also be connected to a PC. A power supply converting AC to DC current will also be employed. Through this section, an analysis of each device characteristics will be given, as well as a short outline of their principles of operation.

When measuring forces, one of the most widespread devices both in the academia and industry are the **load cells** [38]. Due to their variety in principle operations, shape, load type (axial, transversal, torque,...) and capacity (from zero to thousand of tons), plus the possibility of interconnecting them, they cover a wide range of applications. A load cell transforms a force input into an measurable electrical output, with an accuracy up to 0.03% of the applied force. depending on the operating conditions, several working mediums may be selected: hydraulic (suitable for remote locations, no need for a power source), pneumatic (compliant with the highest hygienic and safety standards) and mechanical (low cost, wide

range of forces and shapes).

Almost all of the described load cells types transform the force input at a specific and direction thanks to a strain gauge. A strain gauge is a usually small and flexible electric circuit composed of fine grade wiring attached to the carrying matrix. The load applied will result in the matrix deformation, and therefore in the circuit strain. The resistance in the circuit will vary proportional to the strain, and thus produce a measurable change in the voltage output. An efficient thermal insulation will guarantee that temperature effects on the electric circuit are disregarded, though this effect could be compensated by using several connected load cells in both tension and compression regimes or by designing specific parts of the electric circuit for that aim. An example of a load cell general circuit is shown in *Figure 19*, though many load cells are far more simple.

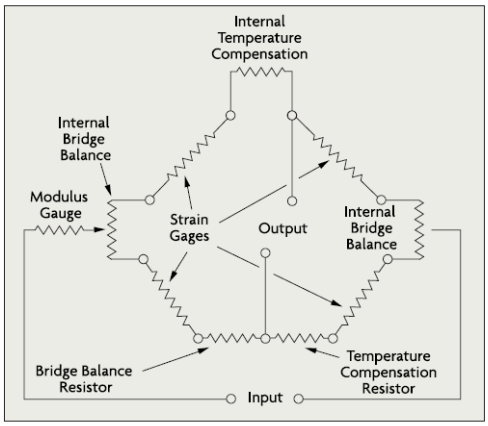

Figura 19: Load Cell Scheme [38]

Several types of load cells are available in the market. Usually, the choice depends on the capacity requirements and the load to be measured, as well as if some spatial restriction is imposed. Some examples are miniature, platform, S-type,... The selected type for the concerning experiment is the beam load cell type, which provides cost-effective measurements for tension-compression loads. A typical beam load cell may be observed in *Figure 20*, with the strain gauges under the white gel (thermal insulation) on both sides of the beam. Threaded holes have been carved on the beam near the edges to facilitate structural load application. The cables colours and meaning will be developed later. The electrical output of the load cell is rated in mV/V, which stands in mV per each V of supplied voltage. As observed, the output is rather small if compared to the power sup-

Figura 20: Load Cell Example

ply. Therefore, either the load cell is connected to high precision measurement device, or the output signal is amplified until measured by most available devices. The second method is preferred. The most usual solution is to connect the strain gauges to a Wheatstone Bridge circuit, which then will be connected to a signal amplifier. Some of the key parameters of a load cell [39] are its capacity (maximum load the device is designed to sustain), precision (accuracy of the cell, rated as a percentage relative to the capacity), non-linearity (maximum deviation from the calibrated 2-point line, expressed as a percentage relative to its fully loaded state), non-repeteability (maximum output difference reported for the same applied weight over multiple runs, expressed again as a percentage relative to its fully loaded state) and operating temperature range. A special remark is given to the safe and ultimate overload (without and with permanent shift in performance characteristics respectively, expressed as a percentage relative to the load cell capacity). Four load cells will be employed in the experiment. Two 5kg ones to measure the axial forces (coincident with the propeller rotating axis) taking place in both the propeller and the sphere, and two 780g ones to measure the torque developed by the propeller (as a mean of a couple of forces). The key parameters of the employed load cells are summarised in *Table 1*, assuming that for the precision and non linearity parameters the highest gain is selected when configuring the Wheatstone Bridge Interface.

Precision	0.05%
Non Linearity	0.05%
Non Repeteability	0.05%
Operating Temperature Range	−20 - 55 °C
Safe Overload	120%
Ultimate Overload	150%

Tabla 1: Load Cell Parameters

A **Wheatstone Bridge** is a widely spread electric circuit invented by Hunter Christie in 1833 and popularised by Sir Charles Wheatstone in the XIX century. It may be considered as a two series-parallel arrangement of resistances, connected to a power supply and grounded (*see Figure 21*). The circuit is usually represented in its rhomboid shape, though rectangular and squared representations may be found in the literature. The circuit will produce zero voltage difference between the parallel branches when balanced [40], which is expressed by *Equation 50*.

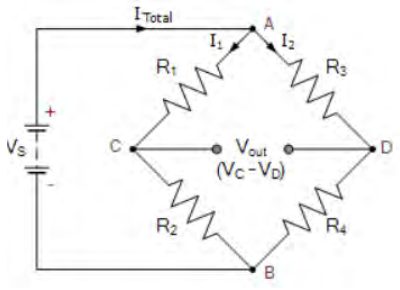

Figura 21: Wheatstone Bridge Example [40]

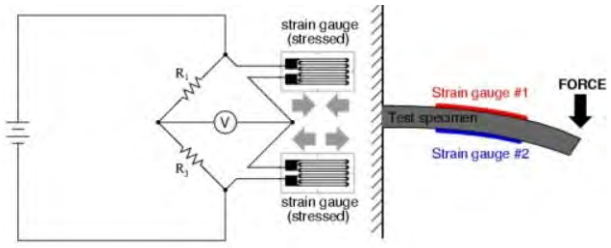

Figura 22: Wheatstone Bridge with Strain Gauge [41]

$$R_1 R_4 = R_2 R_3 \tag{50}$$

Therefore, by substituting the resistances in the wheatstone bridge circuit with strain gauges it is possible to accurately measure their output signal due to the voltage imbalance between the parallel arms. In other words, "*the output voltage variation in the signal diagonal is proportional to the relative variation of the Wheatstone bridge*" [42]. If all resistances are changed, a *full bridge* is obtained. If only two or one are substituted, either a *half bridge* or *quarter bridge* is derived respectively. The load cells employed in this experiment are based on half bridges circuit. In *Figure 22*, a half bridge example for a cantilever beam load cell is shown. As may be observed, one of the strain gauges will work under tension forces, while the other one will do under compression ones, thus counterbalancing possible thermal effects. All in all, the load cell has one input (power supply) and one output (force signal), totalling four wires. The red one accounts for the positive power input (usually 5V, though theoretically may adopt a variety of values), the black for the ground connection and the green and white for the positive and negative signal respectively. This wires are connected to the Phidget Wheatstone Bridge 1046_0 (see *Figures 23*), which operates as the connection element between the load cells (up to 4 different ones) and the user, by an USB connection with a PC.

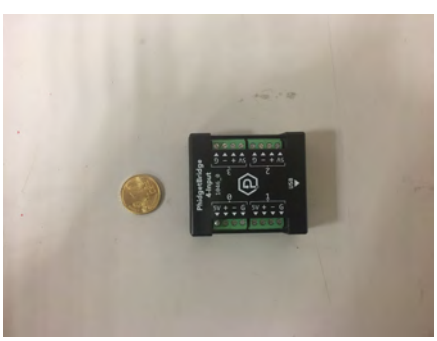

(a) Phidget Wheatstone Bridge 1046_0

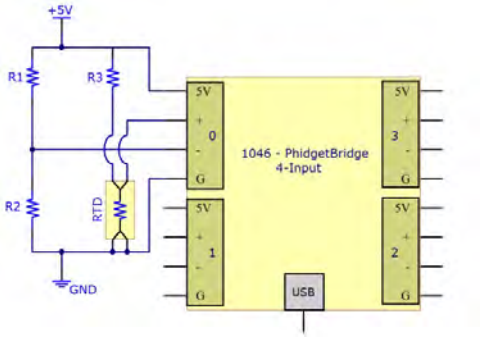

(b) Phidget Wheatstone Bridge 1046_0 Scheme [43]

Figura 23: Phidget Wheatstone Bridge

The Phidget Wheatstone Bridge unit employed in the experiment is shown in

Figure 23a, while an example for the device connection is shown in *Figure 23b*. As may be observed, the connected element is a quarter bridge in which the fourth resistance has been replaced by a RTD (Resistive Thermal Device). Its function is conceptually the same as a strain gauge, a resistance which will change its value based in the operating conditions. While a strain gauge will change its value depending on its physical deformation upon an actuated force or stress (strain), a RTD will vary its value depending on the working temperature. The operation of the Phidget Wheatstone device will be controlled by a software provided by the manufacturing company.

The **Phidgetbridge Wheatstone Bridge Sensor Interface** is the GUI (Graphical User Interface) employed to visualise and control the Phidget bridge device (see *Figure 24*).

Figura 24: Wheatstone Bridge Sensor Interface

This interface allows the user to record the real-time information provided by up to 4 different load cells (among other devices) with user-defined gain and recording rate parameters. The recording rate parameter defines the speed at which the data will be acquired, and is defined as the time interval between two consecutive data records (usually taken in milliseconds). A lower recording rate (lower time interval between records) will imply more data points for a given time interval, yet higher noise in the obtained measurements. This noise may be reduced by adjusting the bridge gain. A higher gain will increase the resolution of the obtained data (hence lowering the noise), yet decrease the measurable output. In other words, a higher gain will restrict the load cell capacity. Thus, a trade off for a given application may be imposed between the desired resolution and the data recording rate. The influence of the gain in both the output range and resolution is shown in the following table (which applies only for the selected device).

Gain	Resolution	Range
1	119 nV/V	±1000 mV/V
8	14.9 nV/V	±125 mV/V
16	7.45 nV/V	±62.5 mV/V
32	3.72 nV/V	±31.25 mV/V
64	1.86 nV/V	±16.652 mV/V
128	0.93 nV/V	±7.8125 mV/V

Tabla 2: Wheatstone Bridge Gain

A gain of 8 and a recording rate of 256 ms is chosen, with a logging frequency of 0.05 s (the lower allowed by the application). The recorded data is saved in a *.log* file which is exported to the *MATLAB* environment in order to post process the data. The file contains five columns: instant at which the data was taken (with accuracy of milliseconds) and value (mV/V) obtained from each load cell (in case there is no load cell connected to the corresponding port, zero value will be shown). Prior to the integration of the load cells into the experiment set up, their calibration needs to be performed. This will allow to find a relation between a load cell output (as mentioned before, rated in mV/V) and the desired output unit (SI force unit was selected). When performing the calibration, coins were chosen due to their availability and known weights (as stated by *Banco de España [44]*, shown in the table below) as well as one lighter which outweighs them. Each load cell was calibrated individually in order to account for each one potential manufacturing defects.

10 cent.	4.10 g
20 cent.	5.74 g
50 cent.	7.80 g
1 €	7.50 g
1 lighter	131.0 g

Tabla 3: Calibration Weights

Through various measurements per load cell, linear relations between the applied weights and the signal output which allows for the conversion between a generic load and the recorded output signal. For each applied weight, the following procedure was followed. The data recording was initialised, and the load cell left unloaded for 5 seconds. Next, the load cell was loaded as smoothly as possible to avoid load peaks in the measurement log. The load is maintained for 10 seconds. Afterwards, it is unloaded and the load cell is left unloaded for another 5 seconds. The Wheatstone Bridge log file, which contains the load cells output (mv/V) over the recording time, is loaded into the *MATLAB* environment. The data are extracted, and the corresponding voltage output value is obtained by averaging the points with greater value than all the obtained values.

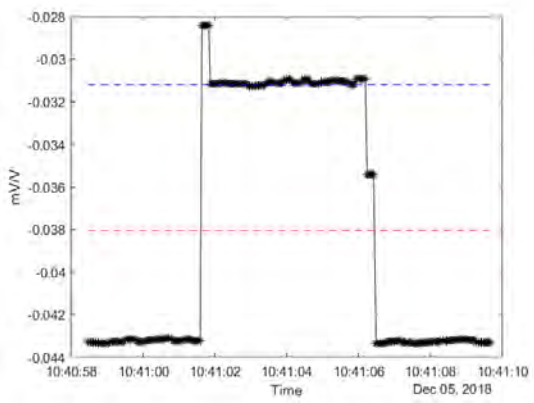

Figura 25: Load Cell Calibration Plot

In other words, an example of calibration procedure is shown in *Figure 25*. The x-axis represents the time at which a data point was recorded, while the y-axis express the output signal yielded by the load cell. Each data point is represented by a black cross, and are connected by the black line. The red discontinuous line represent the mean value of all the recorded points. The average of all the points having higher signal outputs than such mean is assumed to represent the signal output to the applied weight.

The relations, in the form of linear dependency ($y = mx + b$) show good agreement in between the load cells of the same capacity, with the biggest differences happening on each curve offset. A gain value of 8 was selected. The calibration results are obtained in the following relations.

$$W = 57.682\frac{mV}{V} + 0.8413 \tag{51}$$

$$W = 9.886\frac{mV}{V} + 0.431 \tag{52}$$

$$W = 10.189\frac{mV}{V} - 0.598 \tag{53}$$

Where W is the load applied to the load cell (obtained by multiplying the mass of a given weight by the standard gravity constant $g = 9.80655\frac{m}{s^2}$). *Equation 51* refers to a 5kg load cell, while *Equations 52 and 53* do so for the 780g ones. Additionally, another remark was taken into account in the calibration process. Due tot he fact that the load cell was to perform its function in a position which did not allow for an application of a known force (which allows to build the calibration curve relating force and electric signal), it was calibrated in a different position. This is further explained in *Figure 26*.

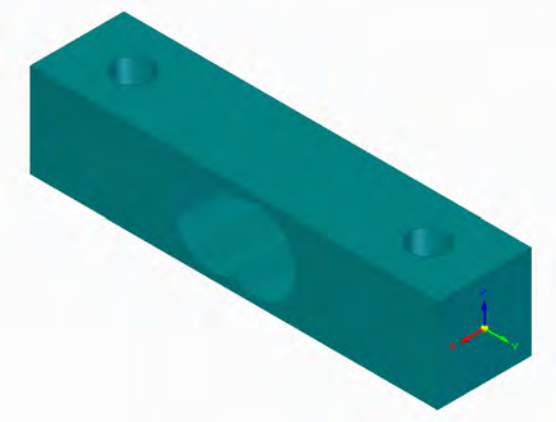

Figura 26: 3D Load Cell Model

The figure above shows a 3D load cell model (in horizontal position) upon which a Cartesian system of reference (with the arrows pointing in the positive direction of the axis) has been placed in order to further clarify the calibration remark. Each load cell is supplied with a sticker on one of its ends representing the direction on which an applied force would produce a positive signal increment with respect to the previous state. In case the previous state was the unloaded one, such increment would result in the applied force. Such arrow takes place in the positive direction of the z-axis (blue arrow). Though the load cell was calibrated in such position, later on it was employed in a vertical position, with the positive direction parallel to the wind direction. Therefore, the load cell signal variation would be related with the sphere drag. However, the calibration data should be corrected, as the measured signals included in that calibration position not only the applied force and electric bias (inherent to the load cell manufacturing process) but also its weight. Such weight associated signal disappears in the set up load cell position, thus being necessary to eliminate it from the data. In order to obtain the bias and weight signal, the data was recorded with the load cell in unloaded state fin four positions, which attending to the direction of the arrow attached to it account for: z-positive, z-negative, y-positive and x-positive directions. According to the arrow direction, each position should give a signal according to the following expressions:

$$S_{z+} = B - W_{LC} = -0.0187$$
$$S_{z-} = B + W_{LC} = -0.0153$$
$$S_{x+} = B = -0.0170$$
$$S_{y+} = B = -0.0169$$

From where instantly follows that the load cell weight signal and electric bias values are:

$$B = -0.017$$
$$W_{LC} = -0.0017$$

Equation 51 has been displayed taken this numbers into account, and thus represents the final equation which will be used to covert the received signal into

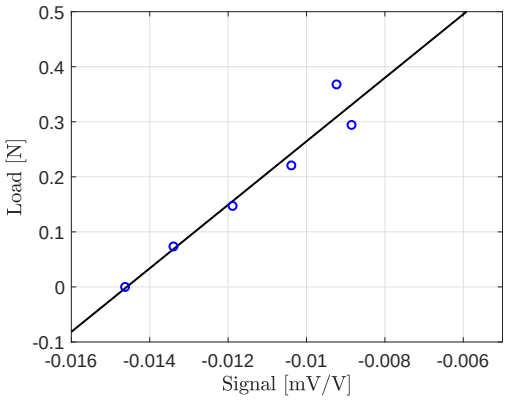

Figura 27: 5 Kg Load Cell Calibration Curve

the applied load. it also has been plotted in *Figure 27* for the user convenience. However, it must be stated that due to this bias and manufacturing defects, load conversion when registering the signal is slightly different in between employing it in the direction indicated by the manufacturer and the opposite one. In other words, calibration curves is slightly different when measuring in z-positive and z-negative axis. The load cell connected to the benchmark data acquisition board is calibrated by the built-in software, displaying directly the propeller thrust.

The propeller (8" in diameter and 4.5" pitch, manufactured in ABS) will be powered by a **Brushless DC** (BLDC) **motor**. A *motor* is a device which is able of transforming the supplied electrical power into mechanical energy, usually in the form of torque (or rotational speed). The difference with the *engines* is that the latter energy supply is of chemical origin (through combustion). Establishing motor categories is a difficult task due to the variables involved (motor structure, control method, physical operation...), though a preliminary taxonomy [45] may arise when comparing their ideal input current, either DC or AC. Inside the DC motors category, the BLDC motor arouse as the natural evolution from the brushed DC motor by achieving electronic commutation by power switches instead of brushes. This holds several advantages, such as higher efficiency and reliability, smaller and lighter motors, greater dynamic response and longer life elements with little maintenance [46]. In order to give a thorough explanation of a BLDC motor, first the physical principles under its operation will be explained, followed by its structure description. Its controlling methods will be conceptually developed when analysing the associated electronic speed controller.

In order to convert the electrical power into mechanical one, BLDC motors run on two main electromagnetic principles. The first one is the Lorentz Law, which states that an electromagnetic force is generated as the consequence of a current I passing through a conductor of length L immersed in a magnetic field of intensity B, with the conductor loop normal vector forms an angle θ with the magnetic field, according to the following relation (influence for an electric field has been assumed negligible):

$$F = q\mathbf{v} \times \mathbf{B} = BIL\sin\theta \tag{54}$$

This force, acting at a distance r from the motor symmetry axis, produces a torque Q on the shaft which may be combined with *Equation 54* in the following relation:

$$Q = 2rFN = K_Q I \tag{55}$$

Where N is the number of conductor coils and I the current intensity. K_Q is called the torque constant of the motor and provides a coefficient relating the output motor torque and current intensity supplied to it.

The second physical principle upon which the motor operation is based is the Faraday Law (see *Equation 56*), which "*describes the voltage induced in a coil of wire in relation to the sum of flux linked by that coil*" [45]. Such voltage is often referred as the back electromotive force (BEMF). Due to the movement of the conductor and the several conductor coils, such voltage is described in *Equation 57*.

$$V(t) = -N\frac{d\phi}{dt} \tag{56}$$

$$V(t) = BLv\sin\theta = K_V\omega \tag{57}$$

Where ϕ is the magnetic flux through each coil, v the velocity of the conductor (which is equal to $r\omega$) and $V(t)$ the BEMF at each time instant. Analogously as with the torque, K_V becomes the coefficient relating the BEMF appearing on the motor and the output rotational speed. This coefficient is usually given by the motor manufacturer and is obtained in unloaded operating conditions.

A BLDC motor is composed of two main structural parts: the rotor and stator. Usually, the stator (non moving part) is placed at the center of the motor, with the rotor (moving part) surrounding it. This is called an *out-runner* motor, and accounts for the majority of motors found in the aeronautical industry. The opposite case (stator surrounding the rotor) is accounts for the *in-runner* motor, more popular on RC cars and trucks applications. As the concerning motor is an out-runner one, its structure will be described. The rotor is the moving part of the motor which will transmit the rotational motion to the propeller, having embedded in it permanent magnets, usually ranging from 2 to 8 poles. It is composed of three part: the can (casing), the permanent magnets and the endcaps (can supporters). On the other hand, the stator is fixed at the centre of symmetry of the motor, and may be classified on single-phase, two-phase or three-phase, depending on the number of winding pairs. It is composed by the stacks (laminated metal pieces holding the wirings), the wirings, a nonrotating shaft supporting the stacks and the bearings. A cross section of a BLDC motor with two permanent magnet poles and three windings single poles three phase stator is shown in *Figure 28*.

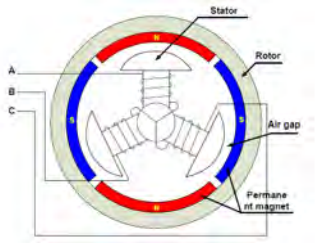

Figura 28: Three Phase Motor Cross Section Example [46]

The operation of a DC motor is conceptually simple. when current flows through one of the stator windings, a magnetic field will be generated which interacts with the permanent magnet poles, generating a force which tends to align them. At the moment they become parallel, current is translated from one winding to the next, thus attracting again the rotor and keeping it in rotation. This process could be helped by introducing an inverse current through the preceding winding, generating a repulsion force which ads to the rotor motion. As stated before, the current control, which for a brushed motor was accomplished by brushes, is performed by electronic means, using a feedback method which may or not include additional sensors (i.e. Hall sensors).

In order to efficiently apply current through the different windings, an **Electronic Speed Controller** (ESC) is needed. The ESC is the electronic device that will control the BLDC motor operation.It usually employs pulse width modulation (PWM) with aide of an H-bridge (see *Figure 30*) in order to convert a constant voltage power source (DC current) into a modulated voltage signal which is directed to the corresponding motor windings. Rising the switching frequency (aiming for a higher motor rotational speed) increases the PWM losses, while lowering it limits the system bandwidth and may rise the ripple current pulses to the point they become destructive [46].

Figura 29: Electronic Speed Controller

The ESC employed is showed in *Figure 29*. As may observed, it is a device designed for operating with currents of up to 12A, though its bust current (maximum current which the ESC may hold for a few seconds without damaging itself, useful at maximum throttle operating conditions) is of 16A according to manufacturer specifications. The three (as the current motor is a three phase one) red cables coming from the bottom of the ESC are the ones which will be connected to the BLDC motor, providing the control of the windings current activation. On the top side, the red and black cables at the sides of the device correspond to the power supply connectors. The power supply may be a series connection of batteries (such as LiPo or NiMh) or a DC one. The cables in the top center place of the ESC account for the linear Battery Elimination Circuit (BEC) wirings. Though years ago it was an optional feature of the ESC, most modern ESC nowadays

come with them, and a variety of different BEC circuits have been developed. Its role is to supply the requested electric signal to power the remaining electronics of the potential RC aircraft (i.e. the transmissor electronics).there are two main types: on one hand, the linear BEC (LBEC) coverts the signal to the required voltage, dissipating the excess energy in heat. Thereby, they do not provide a high efficiency, and if not properly handed, the produced heat may provoke the ESC shutdown. On the other hand, the switching BEC (SBEC) provides the required voltage by means of a PWM method (switching at high frequencies the power source to decrease the input voltage). Though more efficient than a LBEC, the SBEC generates more signal noise. Usually they are set to provide 5V and 1A electric current.

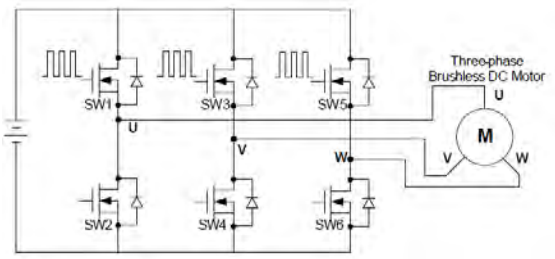

Figura 30: Three Phase H-Bridge

Finally, all the data concerning the BLDC motor operation will be accessed and recorded by the software provided with the **RC Benchmark 1520**. Though the Benchmark originally comes a *ready-to-use* device, including structure and software, as discussed before its structure has been modified in order to make it suitable for its implementation of the wind tunnel. Through this section, the software will be introduced. The different components (motor, ESC, thrust load cell and power supply) are connected to the data acquisition board, which transmits the information received and control parameters to a PC by means of an USB cable. The motor operation will be controlled by the *RC Benchmark GUI* (v1.18) (see *Figure 31*).

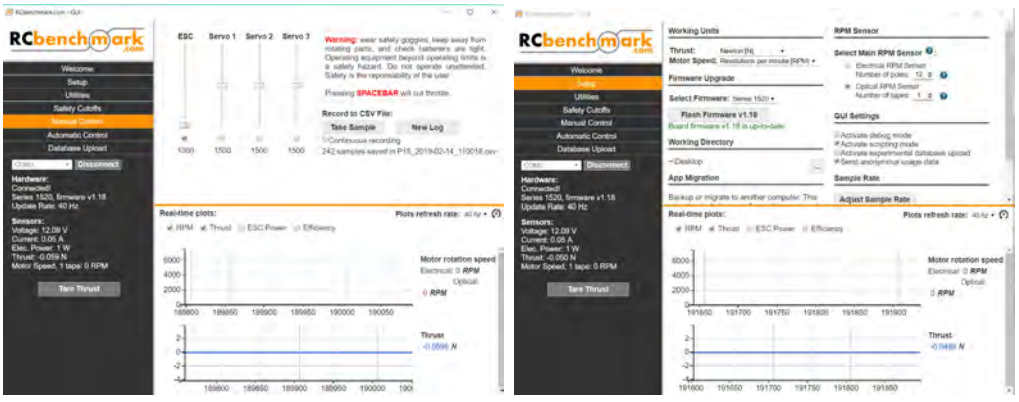

(a) GUI Manual Control (b) GUI Set Up

Figura 31: RC Benchmark GUI

This interface allows the user to record and download the operation data of the motor (thrust, electrical power and angular velocity) and to adjust the velocity at which it will rotate, as well as the duration of the rotation. This may be made by either adjusting an analogue-like throttle switch, either by programming a certain mission profile (the motor would rotate at a given rotation velocity for a given time duration). Such mission profile is finally designed in a *Javascript* script, with the following structure: 1 seconds to initialize the ESC, 4 seconds to increase the angular velocity of the motor from zero velocity to the desired one (the signal associated with such velocity will depend on the wind velocity), 40 seconds of plateau at the given velocity, another 4 seconds to return to the initial rotational velocity and 1 extra seconds to deactivate the ESC and finish the script. Data points are written to a *.csv* file. Safety cutoffs (limits at which, if reached, the GUI will automatically shut down the motor) are user defined and set depending on the motor and ESC limitations. The rotational velocity is originally measured by a sensorless method involving analysing the produced BEMF evolution over time (see *Equation 57*). However, in order to increase the accuracy of such measurement, a magnetic RPM sensor was installed. A magnet was attached to the motor hub. thus rotating with it. Each time the magnet passes near the sensor, an electric signal is produced due to the interaction of the magnetic field with it, which is recorded by the data acquisition board and analysed in order to obtain the rotational velocity measurement.

6.4 Closed Wind Tunnel Corrections

Flow fields and characteristics measurements (i.e. C_D of a bluff body) taken inside a closed loop wind tunnel does not fully resemble the behaviour they will show at their projected operating conditions (open air). This is due to the fact that, being the flow constrained by the lateral walls, any flow will compress and increase its velocity when encountering any object placed inside the tunnel. Such effects has been thoroughly studied, and numerous corrections arise for a various flows (both two and three-dimensional). Additionally, velocity (and, therefore, momentum and energy) dissipation in the vicinity of the lateral walls (boundary layer effects) will to some extent affect the developing airflow. With regards to the concerning experiment, four main corrections have been applied, assuming that the flow is to remain incompressible within the different flow regimes.

First of all, the presence of the slotted profile covering the full length (one of them being the profile on the floor of the test section, the other either the profile supporting the sphere or motor set up) of two lateral walls will influence the velocity fields to some extent by reducing the tunnel cross section area through which the air flows. Such effect is modelled by assuming an effective decrease in the cross section area by means of the massflow conservation through all the tunnel test section:

$$CV_0 = A_1 V_1 \tag{58}$$

With C the original cross section area of the wind tunnel, A_1 the cross sectional area of the test section taking into account both slotted profiles and V_0 and V_1

the associated velocities. Taking into account the slotted profile geometry, the following correcting factor is found.

$$V_1 = \frac{C}{A_1} V_1 = 1.17 V_0 \tag{59}$$

The second correction accounts for the flow blockage induced by the presence of a solid body immersed in such flow. The effect of the motor supporting structure will be considered negligible as it is located after the propeller, and subsequently does not affect the ingested flow. Therefore, the only solid blockage accounted relevant is related with the sphere presence.Due to the flow confinement in the closed tunnel, for low speed flows the flow will accelerate in the proximity of the slid body, therefore increasing its velocity with respect to the one it would achieve in open air operating conditions. As a consequence, the body forces and coefficients measured at the wind tunnel correspond in reality to the ones achieved at a higher freestream velocity in open air conditions. This effective increase in velocity in modelled as a 2-D case taking into account that the solid body is a sphere, assuming axisymmetric flow. The correction employed is extracted from B. Barlow, W. H. Rae & A. Pope [34], which reads as follows:

$$\frac{\Delta V}{V} = \frac{V_c - V}{V} = \frac{K_{sb} V_{sb}}{C^{3/2}} \tag{60}$$

Where V_c is the corrected velocity, V the freestream velocity, K_{sb} the body shape factor (which has been determined experimentally to be equal to 0.96 for a body of revolution) and V_{sb} the body volume.

Next, a correction may be applied to blockage arisen due to the body wake. In an analogous reasoning as before, the presence of the walls constraint interacts with the wake properties, inducing a drag increment in the body by increasing the dynamic pressure. In order to account for this effect, Maskell [35] correction to wake blockage is employed:

$$\frac{\Delta q}{q} = \frac{q_c - q}{q} = K_{wb} \frac{C_D S}{C} \tag{61}$$

Where q_c and q are the corrected and measured flow dynamic pressure, C_D the measured body drag coefficient (which should be re-computed once the dynamic pressure has been corrected), S the frontal area for the wake body source and K_{wb} the wake blockage factor (which is related with the body shape, and equals 2.75 for a body of revolution).

The last applied correction involves the presence of the propeller in the flow. Glauert [36] derived an appropriate correction for the flow in the vicinity of a propeller operating in a closed wind tunnel assuming the ratio of its disk are and the test cross-section is small enough. Due to *Equation 58*, massflow should remain constant through the test section. Due to the streamtube produced when operating a propeller, velocity inside it would be higher than the freestream one, while the velocity out of it would be smaller. However, in open air conditions velocity out of the streamtube would take the freestream value. This difference in velocity (and, consequently, in static pressure) would allow the thrust measured by the propeller in the wind tunnel to be higher than the open air one (or the same as produced

in open air at a velocity V' higher than the freestream tunnel velocity V). The correction relating such velocities is as follows:

$$\frac{V'}{V} = 1 - \frac{\tau\alpha}{2\sqrt{1+2\tau}} \tag{62}$$

Where τ and α are the following parameters:

$$\tau = \frac{T}{S_{prop}\rho V^2} \tag{63}$$

$$\alpha = \frac{S_{prop}}{C} \tag{64}$$

Where T is the measured propeller thrust, ρ the flow density (assumed to remain constant) and S_{prop} the propeller disk area.

6.5 Error Analysis

Due to the experimental nature of the obtained results, it is mandatory to derive the errors committed for each significant parameter. Evaluation of the propulsive efficiency of the set up comes through the analysis of its main non-dimensional parameters: propeller advance ratio (J) thrust (C_T) and power coefficients (C_P), as well as its propulsive efficiency (η) and net force coefficient (C_N). Additionally, the drag coefficient (C_D) evolution of the spheres will be discussed. Each parameter error will be computed according to Moffat [37] error analysis for a multiple sample variable measurement. Such analysis indicates that a given measured variable is expressed by the following expression:

$$X_i = X_i(measured) \pm \delta X_i \tag{65}$$

Where $X_i(measured)$ is the recorded value from that variable and $\pm\delta_i X_i$ is the maximum value its uncertainty may be (generally speaking, the measurement device error, provided by the manufacturer), with very little probability that the variable uncertainty exceeds this value.Analogously, a general result R obtained as the combination of n measured variables X_i may be expressed as the combinations of its measured value ($R(measured)$) and the associated uncertainty($U_{R,0.95}$). Such uncertainty expresses the maximum deviation that may happen from the measured value in a 95% confidence interval.The results would then be expressed as follows:

$$R = R(measured) \pm U_{R,0.95} \tag{66}$$

Where the uncertainty is computed in the following way(based on the root squared sum method):

$$U_{R,0.95} = \left\{(B_R)^2 + (tS_R)^2\right\}^{1/2} \tag{67}$$

Where B_R is the *bias error* of the result, obtained as the root squared sum of all the variables bias errors during the full process of its forming variables X_i, which is composed of the steps of calibration, data acquisition and data reduction. They represent the errors not dependant on the experiment conduction, but inherent to

the experiment equipment. For the current purpose, the last two bias errors will be considered negligible when compared with the calibration error. Such error is usually associated with the tolerance given by the manufacturer for each measuring device.

On the other hand, S_R accounts for the *precision index* of the result, and is obtained as the root squared sum of its variables precision indexes. Such error is associated with the random errors taking place during each variable measurement, where N is the number of samples per measurement. In the same was as with the bias errors, only the precision index of the calibration is taken into account. However, as the instrument has already been calibrated, the precision index for a given measurement is yielded by the following expression:

$$S_{X_i} = \left\{ \sum_{i=1}^{N} \frac{(X_i - \bar{X}_i)^2}{N-1} \right\}^{1/2} \tag{68}$$

The parameter t is the Students distribution multiplier, which for a two tailed distribution, confidence interval of 95% and an average sample population of 400 measurements per variable, takes the value ± 1.965.

Being a general result obtained as a known functions of variables, the final uncertainty may be expressed in the following way:

$$\mathbf{U_{R,0.95}R} = \left\{ \sum_{i=1}^{n} \left(\frac{\partial R}{\partial X_i} \delta B_i \right)^2 \right\}^{1/2} + t \left\{ \sum_{i=1}^{n} \left(\frac{\partial R}{\partial X_i} \delta S_i \right)^2 \right\}^{1/2} \tag{69}$$

With the uncertainties of the selected parameters follow are described by the next expressions:

$$\mathbf{U_{R,0.95}J} = \left\{ \left(\frac{B_V}{nD_{prop}} \right)^2 + \left(\frac{VB_n}{n^2 D_{prop}} \right)^2 \right\}^{1/2} + \\ + t \left\{ \left(\frac{S_V}{nD_{prop}} \right)^2 + \left(\frac{VS_n}{n^2 D_{prop}} \right)^2 \right\}^{1/2} \tag{70}$$

$$\mathbf{U_{R,0.95}C_T} = \left\{ \left(\frac{B_T}{\rho n^2 D_{prop}^4} \right)^2 + \left(\frac{2TB_n}{n^3 D_{prop}^4} \right)^2 \right\}^{1/2} + \\ + t \left\{ \left(\frac{S_T}{\rho n^2 D_{prop}^4} \right)^2 + \left(\frac{2TS_n}{n^3 D_{prop}^4} \right)^2 \right\}^{1/2} \tag{71}$$

$$\mathbf{U_{R,0.95}C_P} = \left\{ \left(\frac{B_P}{\rho n^3 D_{prop}^5} \right)^2 + \left(\frac{3PB_n}{n^4 D_{prop}^5} \right)^2 \right\}^{1/2} + \\ + t \left\{ \left(\frac{S_P}{\rho n^3 D_{prop}^5} \right)^2 + \left(\frac{3PS_n}{n^4 D_{prop}^5} \right)^2 \right\}^{1/2} \quad (72)$$

$$\mathbf{U_{R,0.95}}\eta = \left\{ \left(B_{C_T} \frac{J}{C_P} \right)^2 + \left(B_J \frac{C_T}{C_P} \right)^2 + \left(B_{C_P} \frac{C_T J}{C_P^2} \right)^2 \right\}^{1/2} + \\ + t \left\{ \left(S_{C_T} \frac{J}{C_P} \right)^2 + \left(S_J \frac{C_T}{C_P} \right)^2 + \left(S_{C_P} \frac{C_T J}{C_P^2} \right)^2 \right\}^{1/2} \quad (73)$$

$$\mathbf{U_{R,0.95}C_N} = \left\{ \left(\frac{B_T}{\rho n^2 D_{prop}^4} \right)^2 + \left(\frac{B_D}{\rho n^2 D_{prop}^4} \right)^2 + \left(\frac{2TB_n}{n^3 D_{prop}^4} \right)^2 \right\}^{1/2} + \\ + t \left\{ \left(\frac{S_T}{\rho n^2 D_{prop}^4} \right)^2 + \left(\frac{S_D}{\rho n^2 D_{prop}^4} \right)^2 + \left(\frac{2TS_n}{n^3 D_{prop}^4} \right)^2 \right\}^{1/2} \quad (74)$$

$$\mathbf{U_{R,0.95}C_D} = \left\{ \left(\frac{B_D}{\frac{1}{2}\rho V^2 S_{ref}} \right)^2 + \left(\frac{2DB_V}{\frac{1}{2}\rho V^3 S_{ref}} \right)^2 \right\}^{1/2} + \\ + t \left\{ \left(\frac{S_D}{\frac{1}{2}\rho V^2 S_{ref}} \right)^2 + \left(\frac{2DS_V}{\frac{1}{2}\rho V^3 S_{ref}} \right)^2 \right\}^{1/2} \quad (75)$$

6.6 Project Budget & Regulatory Framework

First, it must be noted that the articles 115 and 116 of the *University Carlos III de Madrid* Statute, as well as the university Charter of Rights and Duties of Students, approved by the Council of Government on March 2004, were followed during all the duration of this bachelor thesis elaboration. On the other hand, rules established by the Spanish Government on the working risks prevention (Law 31/1995) were accounted for and respected. In addition to the costs contemplated in *Appendix A*, the following equipment,staff and amortisations costs were identified:

Concept	Cost [€]	A. Period [years]	Hourly Cost [€/h]	Hours	Total[€]
Wind Tunnel	250000	10	3	70	210
Ultimaker 2+ Extended	3000	3	0.15	80	12
PLA Material	33	-	-	-	33
Matlab Software	35	-	-	-	35
Solid Edge	Free	-	-	-	0
Overleaf	Free	-	-	-	0
Computer	1200	5	0.03	576	18
Laboratory Technician	-	-	15	50	750
Junior Engineer	-	-	20	576	11520

Tabla 4: Additional Costs & Equipment Amortisation

Taking all the costs into account, the cost of the project is of **12946.97 €**.

7 Results & Discussion

Through this section, the obtained results will be presented and discussed. Through *Subsection 7.1*, the whole set up and bluff body drag curves will be shown. In *Subsection 7.2*, the propeller characterisation will be displayed, mainly based on its non-dimensional parameters (thrust and power coefficients, as well as efficiency). Finally, several scenarios will be analysed in *Subsection 7.3*, where the propeller ingests the bodies wake. Such ingestion influence on the system and propeller will be discussed. As a last remark, unless otherwise specified, the following lines format and colour format will be employed for the different figures shown: black and discontinuous for the propeller alone, red and continuous for the smallest sphere, blue and continuous for the medium size sphere and a black continuous line for the largest sphere. If results for the same sphere are being plotted, in an analogous way the colour code becomes: red for the smallest distance, blue for the intermediate one and black for the largest one.

7.1 Preliminary Considerations

Preliminary experiments consisted on testing all the electronic components, each one at a time and all of them together. This testing was performed on both the open and closed loop wind tunnels. Each data measurement is characterised by its scenario (size of the sphere and distance to the propeller), as well as by the rotational velocity of the propeller and wind freestream velocity (which at the end of the day yield the advance ratio of the propeller, key non-dimensional parameter which characterises any propeller operating condition).Two non-dimensional parameters characterise each scenario: the non dimensional distance between the propeller and sphere ($\bar{L} = L/D_{prop}$) and the non dimensional sphere size ($\bar{D} = D_{sphere}/D_{prop}$). Three sphere sizes will be considered ($\bar{D} = 0.25$, 0.5 and 0.75), as well as three distances ($\bar{L} = 0.5$, 1 and 1.5). For each data measurement, the wind velocity and standard deviation of it was measured (as the value obtained comes from the *LabVIEW* application multiple sample reading). For every scenario, 5 rotational velocities will be tested (3000-7000 RPM), while 12 different wind velocities will be applied to the system, associated with the different values governing the power applied to the wind tunnel fans (in percentage derived from the maximum power supplied). Starting at 0%, the power will range from 20 to 70% in 5% power increments.This translated into an effective velocity range of $2.8 - 9.5\ m/s$, This two parameters will allow for the obtention of a wide range of advance ratios, which will characterise the system performance. The preliminary experiments included the drag characterisation of the spheres employed in the rest of the experiment. This will also a allow for a description of the drag evolution in the different scenarios. In order to obtain a proper drag characterisation in the considered velocities range, first the drag evolution of the supporting structure and NACA fairing will be determined (see *Figure 32a*). Next, the drag of the complete bluff body structure will be obtained (see *Figure 32b*). By using those values to infer a quadratic curve with respect with the velocity for both the structure with and without the spherical body, and subtracting them, the drag evolution of the sphere alone is obtained (see *Figure 33*).

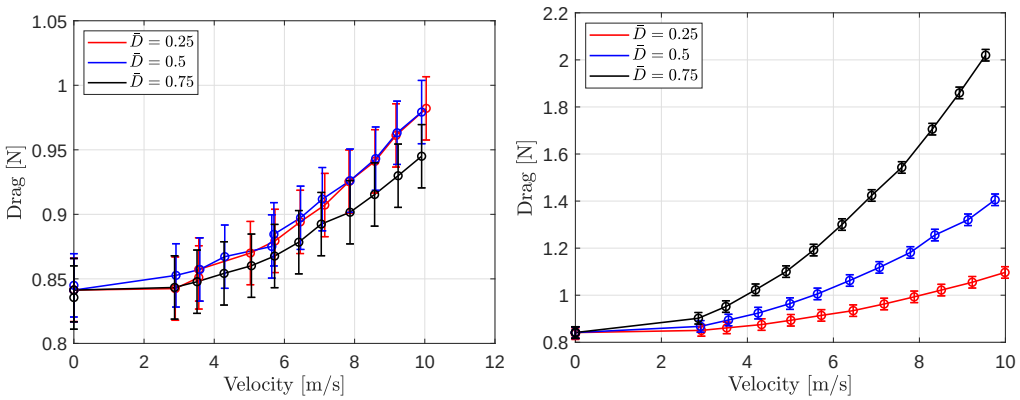

(a) Structure Drag (b) Structure & Sphere Drag

Figura 32: Sphere Support Drag

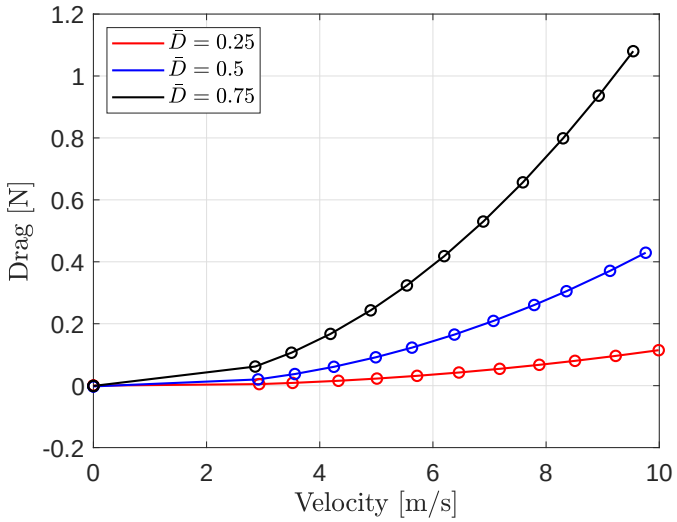

Figura 33: Sphere Drag

Two remarks may be appointed about his figure. First of all, the direction of the load cell measuring the sphere drag is parallel to the wind velocity. In other words, the load cell measurements (through the calibration equation) yields directly the sphere drag. As may be observed, the results shows a good agreement with the theory, as the drag of a body depends on the squared of the velocity and the reference area of it, which for this case such surface was the frontal area of the sphere. The curves depicted illustrates this quadratic behaviour, in the same manner than a bigger spheres yields a higher drag. As the error yielded in the obtention of the half and full structure drag is the same, such error disappears when computing the sphere drag. Additionally, it may be observed in *Figure 32a* that the similarity between the small and medium spheres is due to the fact that both included the fairing, while for the biggest sphere such element only contained a minimum length of it. The following figures show the spheres drag coefficient evolution against both the velocity and Reynolds number (for which the sphere diameter was taken as the reference length).

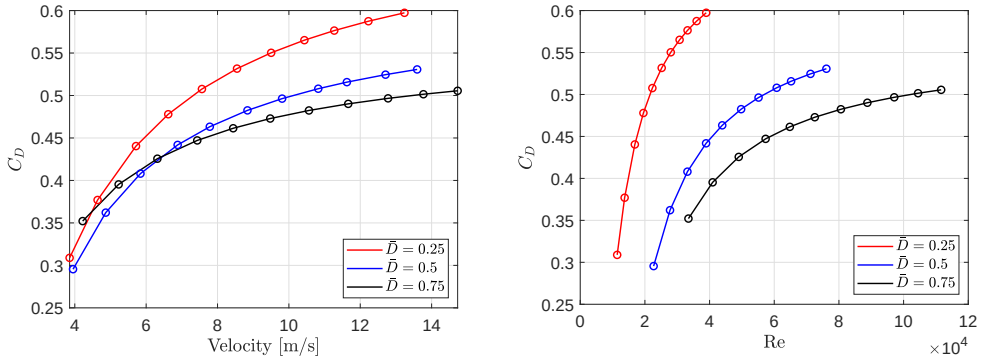

(a) C_D vs V (b) C_D vs Re

Figura 34: Sphere Drag Coefficient

It may be observed that, though the obtained drag coefficient values shown are within the expected order of magnitude for a rough sphere (no surface finish was applied to the sphere as it was considered out of the scope of this paper), which has been shown in the literature to be around 0.5 for this Re number range [47], its evolution does not conform to what has been reported until now in the literature. Expected behaviour was to yield a constant drag coefficient until approximating the drag crisis, which for a rough sphere takes place at approximately 10^5 Re number, where drag coefficient would experience a sudden drop to an approximate value of 0.1. However, as noted by Desphande et. al. [48], the values and evolution of the stages around this drag crisis (subcritical, critical and supercritical) are extremely sensitive to the set up, specially to the sting-to-sphere diameter ratio. Having covered the sting (threaded bar supporting the sphere) with the NACA fairing this could play a strong effect on the drag coefficient evolution. Nevertheless, it should be noted that on the mentioned work the sting was placed on the back of the sphere. This configuration, although far suitable for measuring the sphere drag, was discarded for the present experiment as its influence on the after sphere flow (propeller inflow) would be far too great to effectively asses the sphere influence on the propeller performance, and the time employed on designing such structure would have been too high.

7.2 Propeller Characterisation

Through this section, the propeller characterisation results will be shown. This includes the discussion of the key non dimensional parameters which govern its performance: thrust coefficient (C_T), power coefficient (C_P), and efficiency (η). Such parameters have been computed for a variety of advance ratios (J), based on the rotational velocities at which a specific data point was taken.

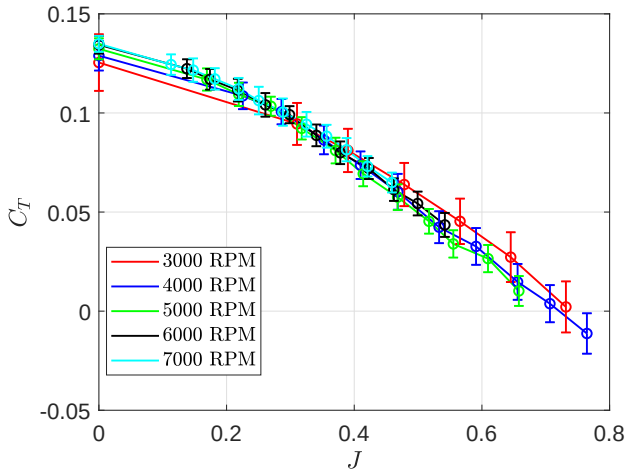

Figura 35: C_T vs J

The thrust coefficient evolution for the propeller is shown in *Figure 35*. As may be observed, this propeller shows a propulsive performance which is almost independent of the rotational velocity. Behaviour shows good agreement with the literature [2], as the curves may be approximated by a first degree polynomial when related to the advance ratio. Maximum thrust coefficient takes a value of around 0.13, with very little variation on the rotational velocity, while the advance ratio at which it becomes zero (no more thrust yielded by the propeller even if the freestream velocity increases) is around 0.6. This advance ratio is identified as J_1. Thus, for the purpose of analysing the propulsive performance of the system, points of interest lies in the region where the propeller is generating thrust. In other words, points of interest advance ratios take values smaller than J_1. It is also remarkable that the measurement errors decrease as the rotational velocity is increased, due to the higher order influence of it on the error analysis method employed. No noticeable dependence is observed on the advance ratio.

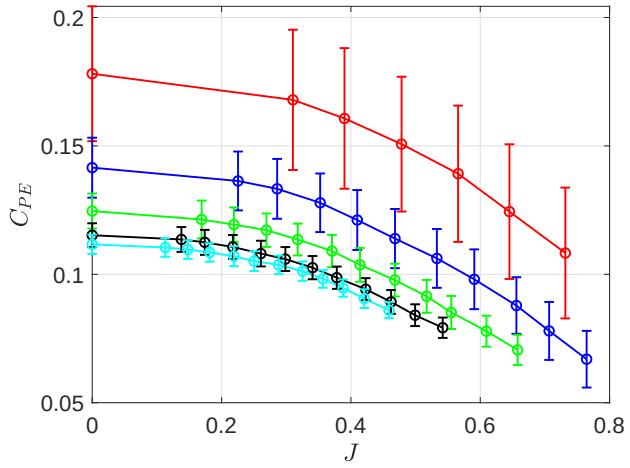

Figura 36: C_{PE} vs J

The propeller power coefficient is shown in *Figure 36*. Due to unidentified

errors with the micro load cell calibration and set up installation, torque values coming from logged from the Wheatstone Bridge are erratic and induce results with little physical sense. Therefore, it was decided to use instead the electric power registered by the RC Benchmark. Such power (obtained according to $P_E = VI$) may be corrected to the actual shaft power delivered to the propeller by multiplying it with the motor efficiency, which is rated by the manufacturer as a maximum value of 80% in optimal conditions. The obtained curves show good agreement with the literature, where it is stated that the power coefficient is approximated with a quadratic relation with the advance ratio. On the contrary when compared with the thrust coefficient, values for the power one show a strong dependence on the rotational velocity, tending to consume less non-dimensional powers as it is increased. On the other hand, the curves tend to converge to the same values as well. Maxima is observed for the 3000 RPM curve at a value of 0.18, while converged maxima value yields approximately 0.11, which holds for both 6000 and 7000 curves. Analogously to the thrust coefficient, measurement errors tend to decrease with increasing rotational velocity, with no noticeable dependence on the advance ratio.

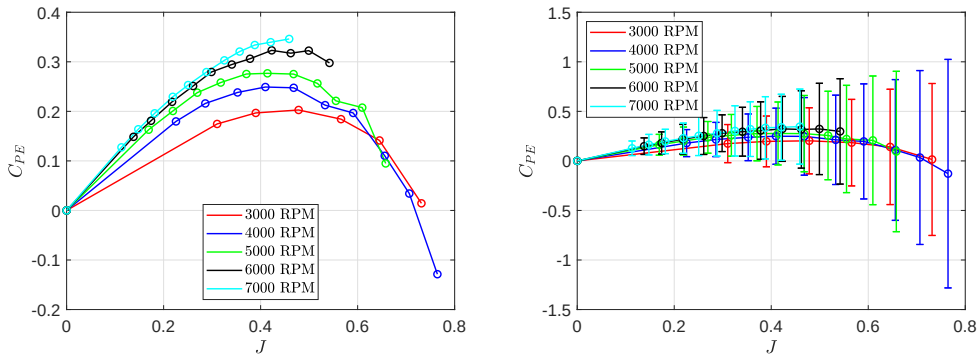

(a) η_E vs J (b) η_E vs J (with errors)

Figura 37: Propeller Efficiency

Figure 37b shows the propeller efficiency distribution with the errors associated with the measurements. As may be observed, errors become incredibly high as the advance ratio increases, which is proportional to the wind freestream velocity, while showing no dependence with the rotational velocity, as happened with the thrust and power coefficients. This is due to the fact that the error method employed does disregards the result partial derivatives sign, which implies that every error adds up. As two out of the three error partial derivatives are directly proportional with the advance ratio, the higher it is, the higher the total error becomes. For the sake of clarity and to more easily discuss the results, measurements without the error bars are shown in *Figure 37a*. It is observable that as the rotational velocity increases, so does the efficiency curves values, which show a quadratic behaviour with the advance ratio, and whose shape is strongly influenced by the $C_T J$ product. After J_1, which would yield zero efficiency values, due to the fact that no thrust is produced (in fact, a negative thrust is registered, meaning that the propeller is reacting like a turbine blade generating power), a negative efficiency is produced. The maximum efficiency value would be around 30% for the 7000 RPM

curve, though it probably would be possible to obtain a higher efficiency value with greater rotational velocities. The value spiking at the right of the figure lying on the 5000 RPM on the curve is possibly due to an error on the measurement procedure. It must be noted that, though on this subsection only selected cases of interest will be discussed, all obtained curves are available at *Appendix C* for the reader convenience.

7.3 Wake Ingesting Scenarios

Through this section, the propulsive system formed by the sphere and propeller will be analysed. Specifically, the change in thrust and power consumption by the propeller will be discussed, as well as its efficiency. In order to identify the governing parameters of this set up, a parametric study of the system will be carried out, based on two main factors as discussed before: the sphere size ($\bar{S}$) and the distance between the sphere and propeller ($\bar{L}$). This parameters combination yields a total of 9 scenarios. For each scenario, measurements were taken varying both the propeller rotational velocity and freestream wind velocity, in the same way the propeller characterisation were performed.

First of all, the dependence of the system performance on the propeller rotational velocity will be discussed. For such purpose, the system performance on a single scenario on the full range of rotational velocities will be displayed. The chosen scenario is characterised by $\bar{D} = 0.5$ and $\bar{L} = 1$.

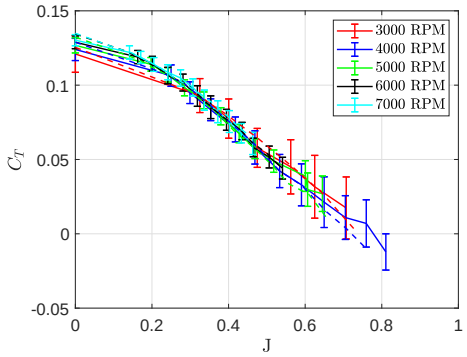

Figura 38: C_T vs J

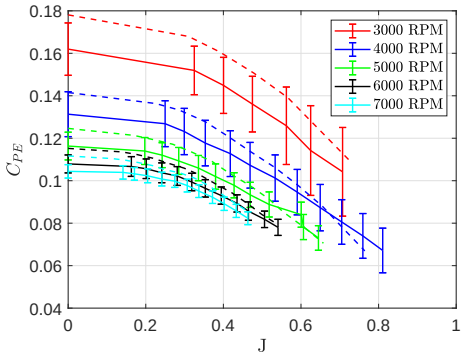

Figura 39: C_{PE} vs J

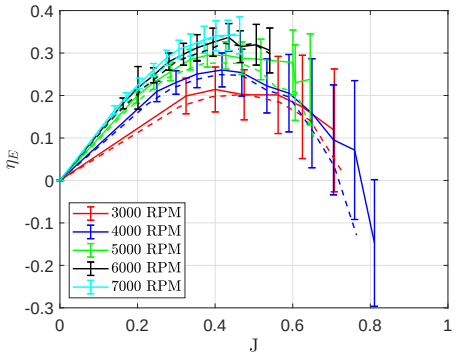

Figura 40: C_{PE} vs J

As may be observed from the figures above, where the dashed lines represent the propeller performance alone and the continuous lines the system performance in the scenario previously described, curves behaviour show no substantial difference when comparing both scenarios. In other words, obtained curves for each scenario, though differing in values, experiences a variation which also takes place for the isolated propeller,so it may be safely assumed that the rotational velocity plays no substantial role on the propeller performance variation for the phenomena to be studied (wake ingestion). Therefore, from now on when analysing the two other parameters, as the influence of the rotational speed is negligible on the system propulsive performance, the results will be shown for a symbolic rotational speed of 5000 RPM. The system dependence on the non-dimensional distance is now shown and discussed. For such purpose, the key parameters will be displayed grouped by its non-dimensional sphere size.

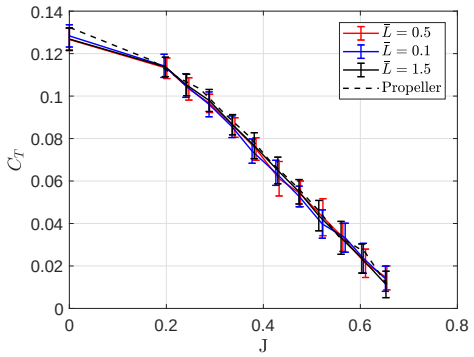

Figura 41: C_T @ $\bar{D} = 0.25$

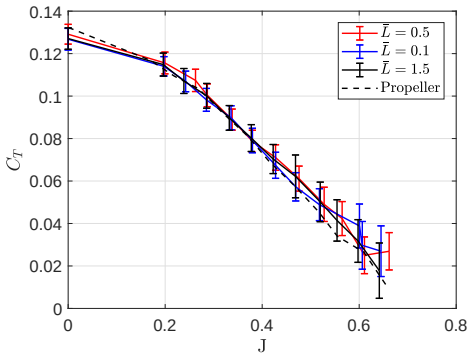

Figura 42: C_T @ $\bar{D} = 0.50$

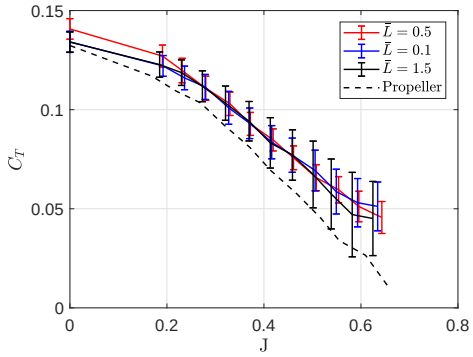

Figura 43: C_T @ $\bar{D} = 0.75$

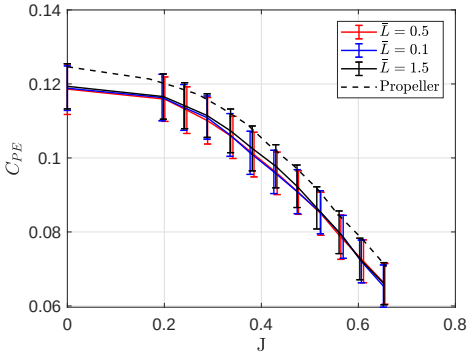

Figura 44: C_{PE} @ $\bar{D} = 0.25$

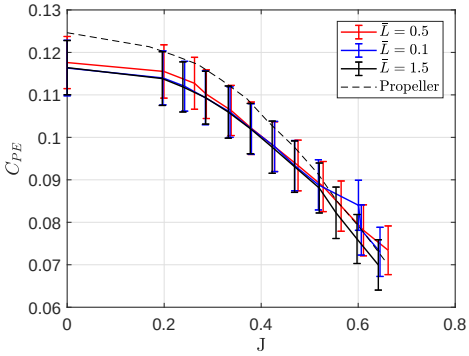

Figura 45: C_{PE} @ $\bar{D} = 0.50$

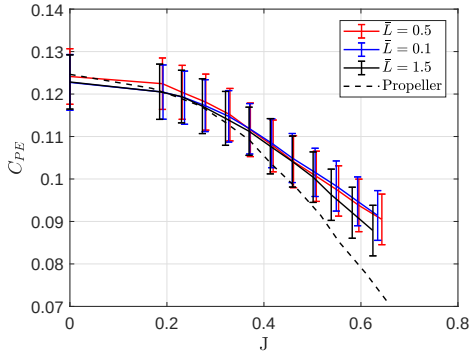

Figura 46: C_{PE} @ $\bar{D} = 0.75$

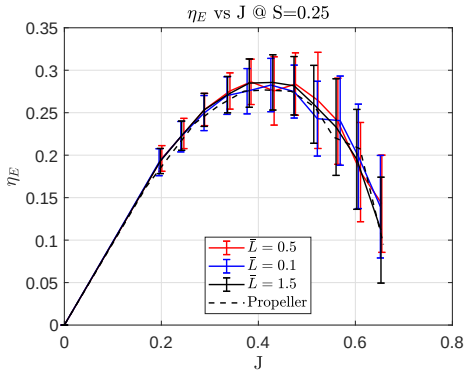

Figura 47: η_E @ $\bar{D} = 0.25$

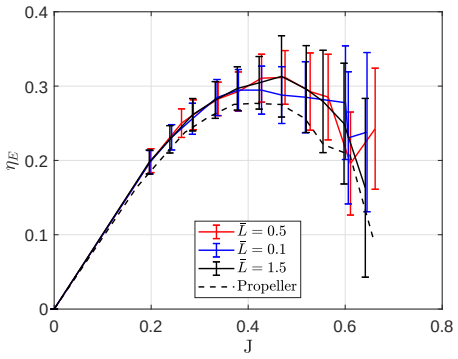

Figura 48: η_E @ $\bar{D} = 0.50$

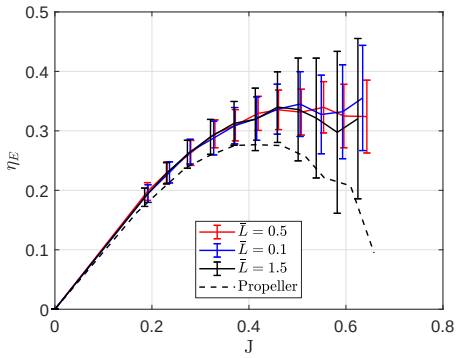

Figura 49: η_E @ $\bar{D} = 0.75$

Through *Figures 41, 42 & 43* the thrust coefficient evolution is displayed for each sphere, considering the three distances covered. The same analysis is observed for the power coefficient (*Figures 44, 45 & 46*) and for the efficiency (*Figures 47, 48 & 49*). The conclusion which may be inferred from these figures is that for the ranges of distances covered, no difference is observed on any sphere on the effect they produce on the system performance depending on the distance between them. In fact, curves are coincident for almost all the concerning advance ratio range, except for the final advance ratios considered, which imply the highest freestream velocities employed in the experiment, where measurements start to diverge. Therefore, it may be drawn that the non-dimensional parameter $\bar{L}$ is not determinant in assessing the influence of a wake ingestion on the propeller performance, at least for the advance ratios range considered in this experiment. This fact may be due to the short distance in between the sphere and the propeller (up to $\bar{L} = 0.75$), which gives little room for the sphere wake to develop and affect in a substantially different manner the propeller performance between the considered distances. Thus, in order to assess the influence of the sphere size ($\bar{D}$) on the propulsive unit performance, the non-dimensional parameters will be plotted for the distance $\bar{L} = 1$.

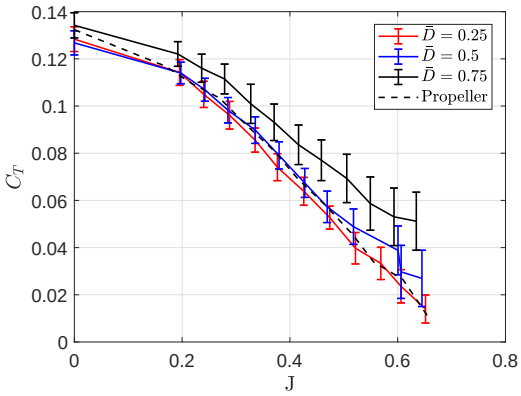

Figura 50: C_T vs J @ $\bar{L} = 1$

Figure 50 shows the thrust coefficient evolution of the propeller depending on the sphere size. Unlike the rotational velocity and the distance between the sphere and propeller, the sphere size induces important changes on this coefficient. While the small and medium size spheres ($\bar{S}$ of 0.25 and 0.5 respectively) produce approximately the same reduction in thrust coefficient, thus providing less thrust overall except for high advance ratios where the medium sphere increases the thrust yield, the large sphere induces a higher thrust production over all the advance ratio range. This is due to the momentum defect induced by the presence of the sphere with respect to the freestream flow. According to the power balance method introduced previously, the sphere presence would modify the incoming flow which serves as input for the propeller, increasing the difference with the reference flow (freestream one), and thus increasing the term $\dot{E}_{in,a}$ in *Equation 16*. Such increase would result in an increment in the TV_∞ term. The other terms involved (outflow wake) would be reduced as they approach freestream conditions. On the other hand, a simpler explanation rise from propeller theory and the propeller characterisation, it has been shown that more thrust is produced the lower the freestream velocity at a fixed rotational velocity. Therefore, lowering the velocity the propeller ingests would incur in a higher thrust. This conditions does not apply to the other spheres. This is due to the fact that in order to comply with the mass conservation theorem inside the wind tunnel, fluid outside the sphere wake increases its velocity, in opposition to the fluid in the wake, which decelerates. This accelerated fluid goes through the part of the propeller which generates the most thrust, which lowers its performance (the nearer to the root the propeller cross section is, the lower its thrust generation capacity and thicker it would be in order to comply with structural reasons).

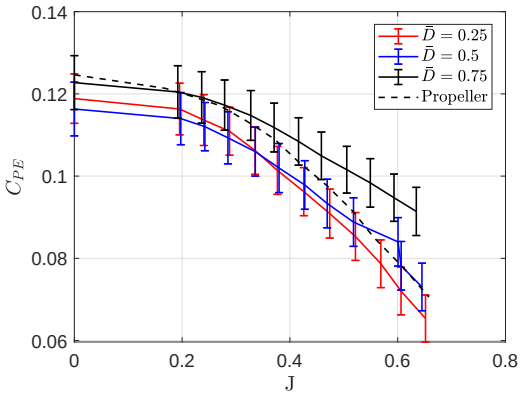

Figura 51: C_{PE} vs J @ $\bar{L} = 1$

A similar tendency as with the thrust coefficient is observed with the power coefficient on *Figure 51*. While the two smaller spheres clearly show a reduction in the power consumption, the larger one exhibits almost the same power consumption as the isolated propeller, though the non-dimensional power increases with the advance ratio for this sphere. In fact, this energy conversion mechanism is also explained by *Equation 16*. While it was shown before that for the largest sphere the increase in the incoming wake energy was employed to increase the yielded thrust, it is observable that for the smallest spheres such energy increment is used to reduce the power consumption while slightly lowering the thrust production. Again, propeller theory supports this claim, as the more aerodynamic part of the propeller (nearer the tip) ingests an accelerated flow, the power needed to maintain its rotational speed is lowered. However, the way in which each power conversion mechanism appears (either thrust production increase or power consumption reduction) remain uncertain, though the concerning experiment induces that it is deeply related with the system geometry. In such way, the results from the current experiment suggests that such mechanism is deeply related with the non dimensional parameter $\bar{D}$. Therefore, a more exhaustive parametric study to assess the influence of this parameter on the power saving mechanism becomes a possible investigation line.

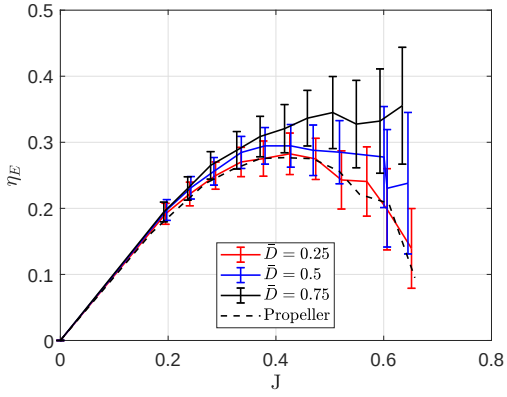

Figura 52: η_E vs J @ $\bar{L} = 1$

Regarding the propeller efficiency evolution (see *Figure 52*), it remarkable

the fact that no matter the power conversion mechanism, the propeller achieves a higher efficiency at all points of the advance ratio range considered, with maximum observed increments of up to 14, 19 and 44% in efficiency for each sphere respectively, and similar figures. This efficiency increase is more remarkable at higher advance ratios, though the increment in measurement errors does not allow for a solid statement on this aspect. This increase in efficiency comes as a consequence of the power conversion mechanisms previously discussed. If either the thrust coefficient is increased ($\bar{D} = 0.75$) or the power coefficient is decreased ($\bar{D} = 0.25$ & 0.5) while the other parameters do not suffer substantial changes, propeller efficiency will increase. However, the drawback of this efficiency is that omits part of the system, as only takes into account the propulsive unit (propeller), while ignoring the bluff body or wake generating system (sphere). This global performance of the system may be assessed by the net force coefficient (C_N), which is deeply involved not only with the thrust evolution across the different scenarios but with the body drag behaviour when paired with the propeller unit.

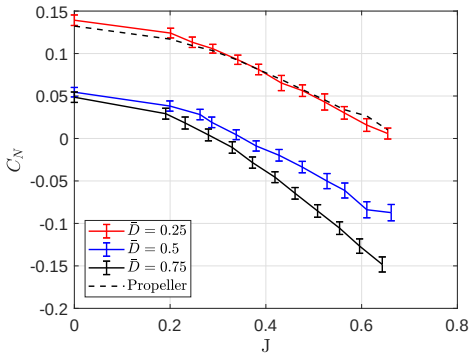

Figura 53: C_N @ $\bar{L} = 0.5$

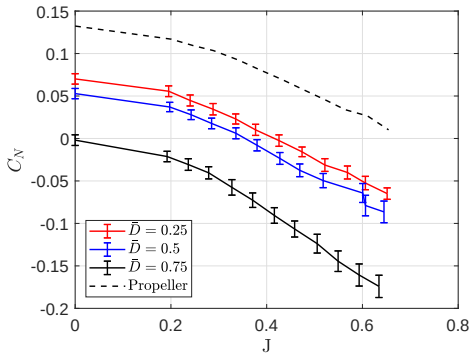

Figura 54: C_N @ $\bar{L} = 1$

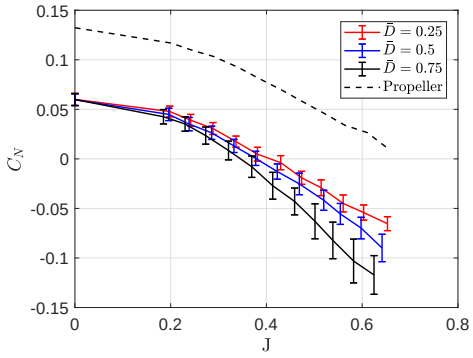

Figura 55: C_N @ $\bar{L} = 1.5$

Figures 53, 54 & 55 shows the net force coefficient evolution for all the scenarios grouped by the non dimensional parameter $\bar{L}$. Though it was demonstrated that such parameter plays no role on the propeller performance, it does affect the whole system behaviour, as the distance between the propulsive unit and the bluff body exerts a noticeable modification on the drag experienced by the body. This effect is acknowledged in the literature [18] [19]. It may be observed that the net thrust

coefficient of the system is much lower than the thrust coefficient of the isolated propeller, due to the inclusion of the sphere drag force on the computations. Under this coefficient, a zero value would imply the equilibrium position ($T = D$) on which the system would travel at constant velocity equal to the freestream one. The advance ratio at which this condition holds increases as the distance between the propeller and sphere increases, due to the decreasing effect of the propeller on the sphere drag.However, it may be noted that equilibrium condition is achieved for the concerning experiments around the advance ratio 0.4, meaning that before such point the whole system would be able to generate some thrust. In addition, the coefficient is observed to increase the smaller the parameter $\bar{D}$ is, as a consequence of the smaller drag produced by the whole system. Therefore, in order to optimise this coefficient, the body system drag behaviour should be fully determined. Such behaviour for the concerning experiment will be described in the next paragraph. Nevertheless, this coefficient optimisation should be assessed as part of the power balance taking place for the whole system, in order to account as well for the aircraft power optimisation as well. As a last remark, it must be noted that for the smallest sphere ($\bar{D} = 1$) in the closest scenario ($\bar{L} = 0.5$) the net force coefficient is almost identical to the isolated propeller thrust coefficient. This is due to the fact that the sphere wake is ingested on the vicinity of the propeller hub region, therefore not affecting at all to the propeller performance.

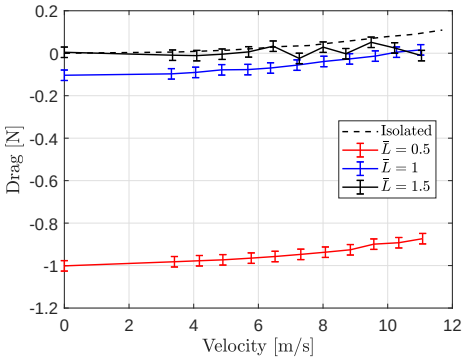

Figura 56: Drag Evolution $\bar{D} = 0.25$

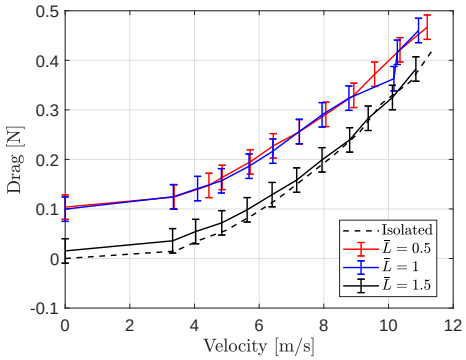

Figura 57: Drag Evolution $\bar{D} = 0.5$

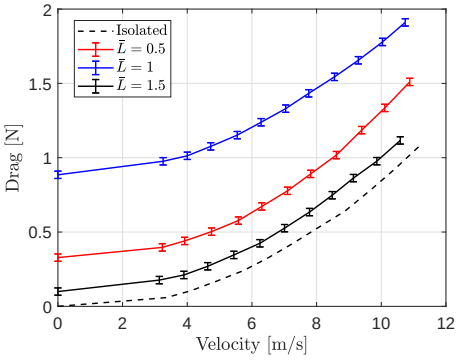

Figura 58: Drag Evolution $\bar{D} = 0.75$

As may be observed from *Figures 56,57 & 58*, the drag evolution of the different spheres over the considered scenarios is rather erratic, with little correlation in

between the smallest sphere, and the other two. While for the medium and largest spheres it is remarkable the fact that the total drags registered increase the closer the sphere is placed to the propeller, the mechanisms by which this occurs remain unclear. The global increase though may be attributed to the thrust increase at equilibrium condition, causing an extra suction on the body which increases the body pressure drag. On the other hand, it is noticeable the fact that the higher the sphere size ($\bar{D}$), the higher the drag increase. Thus, the evolution of the drag force, and, therefore, of the net thrust coefficient, holds a dependence on both $\bar{L}$ and $\bar{D}$.

8 Conclusions

The aviation world is rapidly changing and holds probable scenarios where a growth in the number of travellers will place on the aeronautical industry an increasing load in the manufacturing not only of more aircrafts (talking in shear numbers), but of more modern aircrafts. Such vehicles should be able to address the incoming technological challenges in terms of efficiency, fuel consumption, capacity and noise. On the other hand, the introduction of new types of aircraft in both military and civil aircraft, namely UAV, imposes new challenges from the engineering point of view, often due to completely different vehicle sizes and mission profiles.

In order to provide an answer to the numerous emerging challenges, new technologies and concepts are being investigated upon, one of the most promising being the wake or boundary layer ingestion. This phenomena takes place whenever the aircraft propulsive system ingests an airflow which differs from the freestream one either in velocity, pressure or both. Such airflow may arise from a bluff body placed in front of it or, for the more advanced aircraft conceptual designs, from the ingestion of its own airframe boundary layer. This phenomena has gained importance by novel designs pushing for a more system integrated aircraft construction.

The present paper aims to investigate upon such phenomena in order to yield a better comprehension of the mechanisms underlying it. For such purpose, the experimental procedure presented is designed and carried out to assess the influence of two main parameters on a simplified aircraft concept, which may e divided on two systems: propulsion subsystem and body subsystem. The chosen propulsion system is a propeller paired with a BLDC motor, while the body systems are comprised of three 3D printed spheres. The main parameters are the non dimensional distance between the propulsion unit and the body unit, and the non dimensional size of the sphere. Both quantities have been made non dimensional with the propeller diameter. A parametric study was performed on a close loop wind tunnel for a variety of freestream wind speeds and propeller rotational velocities. Reynolds numbers considered range from 10^4 to 10^5. 9 scenarios were considered, aside from the propeller characterisation and drag analysis of the bluff bodies, arising from the three sphere sizes and the three distances between body units and propellers. Results were discussed from the propeller theory and Drela [14] power balance method.

The obtained results show that the influence of the non dimensional distance between propeller and sphere is negligible, yielding curves which are almost identical for the studied advance ratios range. On the other hand, influence of the sphere size on the propeller performance becomes the dominant parameter, which is related with the produced body wake size. This body wake would alter the propeller incoming flow, which translates into a momentum defect from the freestream reference flow. Such defect is considered as a energy source which positively affects the propeller performance. However, the performance improvement is found to be dependant on the non dimensional sphere size, yielding two energy conversion mechanisms. Performance enhancement is produced either

by increasing the propeller thrust or by reducing the power consumption at for the majority of the considered operating conditions range. Though propeller performance (both in terms of thrust and power coefficients, as well as efficiency) is improved by the presence of the wake inducing bodies, in order to assess the whole system performance it is preferable to analyse the net force coefficient. Such coefficient is observed to increase the smaller the non dimensional sphere size.

8.1 Future Work

To close this paper, the main possible lines of investigations which could be derived from this experiment will be pointed out and summarised. First of all, in order to fully determine the influence of the parameter $\bar{D}$ on the propulsion system performance improvement, as well as its possible determination of the mechanism under which it works (major thrust production or minor power consumption) a thorough parametric study centred on this parameter is suggested. Employed spheres should be increased, allowing for a wide enough range of sizes to be covered, as well as incrementing the advance ratios range considered. On the other hand, this experiment was designed in order to respect as much as possible the flow axisymmetry, and trying to reduce as much as possible other elements interference on the flowfield, specially on the space between the propeller and the sphere. Once the relations between the sphere and the propeller performance are fully determined, the next step would be to employ simple bodies which would incur in fully three dimensional flows which may be closer to real applications (i.e. a cylinder or streamlined body). In addition, it would be of interest to pair the propeller with a wing like structure in its vicinity, in order to assess the influence of boundary layer ingestion on its performance. At the same time, another investigation line goes through characterizing the flow field in the control volume (by PIV or anemometry measurements), to further comprehend power conversion mechanisms.

9 Bibliography

References

[1] *Celebrating a Century of Flight*, National Aeronautics and Space Administration, USA, NASA Publication SP-2002-09-511-HQ, 2003

[2] R. Von Mises, W. Prager, G. Kuerti & K. H. Hohenemser, *Theory of Flight*, New York: Dover Publications, 1959

[3] *FAA Forecast Fiscal Years 2014 - 2034*, Targeted News Service, Washington D.C., USA, March 13 2014

[4] *Airbus Global Market Forecast 2010 - 2029*, Airbus Group, Toulouse, 2010

[5] Bart Custers et al., *The Future of Drone Use: Opportunities and Threats from Ethical and Legal Perspectives* , New York : Springer Berlin Heidelberg, 2016

[6] *European Aviation in 2040 Challenges and Growth*, Eurocontrol Statistics and Forecast Service, 2018, 2^{nd} edition

[7] A. de Juniac, *Annual Review 2018*, International Air Transport Association, Sydney, June 2018

[8] *Flightpath 2050: Europe's Vision for Aviation*, Report of the High-Level Group on Aviation Research, Publications Office of the European Union, 2011

[9] *Strategic Research and Innovation Agenda - Volume 1*, Advisory Council for Aviation Research and Innovation in Europe, 2012, updated on 2017

[10] E. Greitzer et al., *N+3 Aircraft Concept Designs and Trade Studies, Final Report - Volume 1*, NASA, USA, NASA/CR-2010-216794-VOL1

[11] R. Wahls, *N+3 Technologies and Concepts - Integrated Solutions for Fuel, Noise and Emission Reduction*, Green Aviation Summit, NASA Ames Research Center, September 8-9, 2010

[12] A. Betz, "Interference between Propeller and Vehicle: The Ducted Propeller", *Introduction to the Theory of Flow Machines*, Pergamon, New York, 1966

[13] L. Smith, "Wake Ingestion Propulsion Benefit", *Journal of Propulsion and Power*, Vol 1, Nº1, 1993

[14] M. Drela, "Power Balance in Aerodynamic Flows", *AIAA Journal*, Vol 47, Nº7, July 2009

[15] A. Arntz, O. Atinault and A. Merlen, "Exergy-Based Formulation for Aircraft Aeropropulsive Performance Assessment: Theoretical Development", *AIAA Journal*, Vol 53, Nº 6, June 2015

[16] D. S. Scott, "Exergy", *International Journal of Hydrogen Energy*, Vol 28, 2003, pp. 369 - 375

[17] Z. Rant, "Exergie, ein neues Wort für technische Arbeitsfähigkeit", *Forschung im Ingenieurwesen*, Vol 22, Nº 1, 1956

[18] P. Lv et al., "Performance Analysis of Wake and Boundary-Layer ingestion for Aircraft Design", *Journal of Aircraft*, July 2016

[19] P. Lv et al., "Experimental Investigation of the Flow Mechanisms Associated with a Wake-Ingesting Propulsor" *AIAA Journal*, Vol 55, Nº4, April 2017

[20] A. Uranga et al., "Boundary Layer Ingestion Benefit of the D8 Transport Aircraft", *AIAA Journal*, Vol 55, nº 11, August 2017

[21] D. J. Arend, G. Tillman and W. F. O'Brien, *Generation After Next Propulsor Research: Robust Design Embedded Engine Systems*, 48^{th} AIAA/ASME/SAE/ASEE Joint Propulsion Conference & Exhibit, Atlanta, Georgia, 30 July - 01 August 2012

[22] A. Arntz, O. Atinault, "Exergy-Based Performance Assessment of a Blended Wing-Body with Boundary Layer Ingestion" *AIAA Journal*, Vol 53, Nº 12, December 2015, DOI: 10.2514/1.J054072

[23] M. Corral, "Line and Surface Integrals" *Vector Calculus*, Livonia, MI: Michael Corral 2008

[24] G. de Oliveira, R. B. Pereira, D. Ragni, F. Avallone, G. van Bussel, "How does the presence of a body affect the performance of an actuator disk?" in *The science of Making Torque from Wind - TORQUE 2016*, DOI: 10.1088/1742-6596/753/2/022005

[25] J. Andersson, A. Eslamdoost, A. Capitao Patrao, M. Hyensjö, R. E. Bensow, "Energy Balance Analysis of a Propeller in Open Water", *Ocean Engineering*, Vol 158, 2018, pp. 162-170

[26] S. Franchini and O. López, *Introducción a la Ingeniería Aeroespacial*, 2^{nd} ed., Madrid: IBERGARCETA PUBLICACIONES S.L., 2012

[27] S. N. Krivoshapko and V. N. Ivanov, "Helical Surfaces"**in** *Encyclopedia of Analytical Surfaces*, Cham, Switzerland: Springer 2015, pp. 225 - 258

[28] M. T. Schobeiri, "Turbine and Compressor Cascade Flow Forces" and "Losses in Turbine and Compressor Cascades" in *Turbomachinery Flow Physics and Dynamic Performance*, 2^{nd} ed., College Station, Texas, USA: Springer, 2011, pp. 145 - 229

[29] J. S. Carlton, *Marine Propellers and Propulsion*, 3^{rd} ed., Amsterdam : Elsevier 2012

[30] J.B. Brandt, R.W. Deters, G.K. Ananda, and M.S. Selig (15/01/2019), *UIUC Propeller Database*, University of Illinois at Urbana-Champaign, retrieved from http://m-selig.ae.illinois.edu/props/propDB.html.

[31] J. Scott. "NACA Airfoil Series". Aerospaceweb, http://www.aerospaceweb.org/question/airfoils/q0041.shtml , (**accessed: 22 January, 2019**)

[32] L. Houang, "Dynamics" **in** *A Concise Introduction to Mechanics of Rigid Bodies Multidisciplinary Engineering*, New York: Springer, 2012

[33] Ultimaker B.V., Netherlands, "Ultimaker 2 Extended+ Specification Sheet"

[34] J. B. Barlow, W. H. Barrow & A. Pope, "Boundary Corrections II: Three Dimensional Flows" **in** *Low Speed Wind Tunnel Testing*, New York: John Wiley & Sons, 1999

[35] E. C. Maskell, "A Theory of the Blockage Effects on Bluff Bodies and Stalled Wings in a Closed Wind Tunnel", Aeronautical Research Council and Memoranda, Ministry of Aviation, London, Rep. 3400, November 1963

[36] H. Glauert, "Wind Tunnel Interferences on Wings, Bodies and Airscrews", Aeronautical Research Committee Reports and memoranda, Air Ministry, London, Rep. 1566, September 1933

[37] R. J. Moffat, "Describing the Uncertainties in Experimental Results", *Experimental Thermal and Fluid Science*, 1:3-17, 1988

[38] *How to evaluate and Install a Load Cell*, OMEGA Engineering, Connecticut, 2015

[39] *Datasheet Micro Load Cell (0 - 5 Kg)*, Phidgets Inc., 2016

[40] "Wheatstone Bridge" in *Electronics Tutorials* [Online], URL: https://www.electronics-tutorials.ws/blog/wheatstone-bridge.html

[41] "Strain Gauge" in *Neuroscience and Robotics Lab* [Online], URL: http://hades.mech.northwestern.edu/index.php/Strain_Gauge

[42] D. M. Ștefănescu, "Wheatstone Bridge - The Basic Circuit for Strain Gauge Force Transducers" in *Handbook of Force Transducers: Principles and Components*, Berlin: Springer, Part II, Chapter 14, pp. 347 - 358, ISBN: 978 - 3 - 642 - 18295 - 2

[43] *1046 User Guide*, Phidgets Inc, August 2018, [Online] Available: https://www.phidgets.com/docs/1046_User_Guide#Using_a_Wheatstone_Bridge

[44] Banco de España, *Las medidas de Seguridad*, https://www.bde.es/bde/es/areas/billemone/Publico_general/Monedas_de_euro/seguridad/Las_medidas_de_seguridad.html (Accessed Jan 14, 2019)

[45] J. Mevey, "Sensorless Field Oriented Control of Brushless Permanent Magnet Synchronous Motors", Dept. of Electrical and Computer Engineering, Kansas State University, Manhattan, Texas, 2009

[46] *Brushless DC Motor Fundamentals Application Note*, Monolithic Power, San Jose, CAL, USA, 2014

[47] N. Hall, "Drag of a Sphere", National Aeronautics and Space Administration, May 05 2015. Accessed: February 18 2019 [Online]. Available: https://www.grc.nasa.gov/www/k-12/airplane/dragsphere.html

[48] R. Deshpande, V. Kanti, A. Desai, S. Mittal, "Intermittency of laminar separation bubble on a sphere during drag crisis", *Journal of Fluid Mechanics*, vol 812, pp815-840, Jan 2017, DOI: 10.1017/jfm.2016.827

A Appendix I - Inventory

Prices in euros [€] unless otherwise specified.

Product Name	Price (€)		Qty.	Supplier	Product Reference
	Excl. Taxes	Incl. Taxes			
RC Benchmark 1520	148, 18	179, 2978	1	Hobby King	827000001-0
Brushless Rotor Motor 1000 K_v 15A	23.57	28.52	1	Robotshop	RB - May - 38
Lynxmotion 12A Multirotor ESC	15.25	18.45	1	Robotshop	RB - May - 39
Wheatstone Bridge (with enclosure)	79.41	96.09	1	Robotshop	RB - Phi - 378
Flowbotics App (Wheatstone Bridge Interface)	3.45	4.17	1	Robotshop	RB - Phi - 75
8" x 4.5" Propeller Pair	2.93	3.54	1	Robotshop	RB - Gem -10
Switching Power Supply 12V 10A	10.56	12.78	1	Robotshop	RB - Miw - 08
5 Kg Micro Load Cell	6.81	8.24	1	Robotshop	RB - Phi - 118
780 g Micro Load Cell	5.83	8.05	2	Robotshop	RB - Phi - 117
Magnetic RPM Sensor	8.12	9.83	1	Robotshop	RB - Eag - 13

Tabla 5: Electronic Components Inventory

Product Name	Qty.	Supplier	Product Reference
Basic profile 30x30mm, 8mm slot	3.732 [m]	Fasten Sistemas	5010
Hammer head nut	12	Fasten Sistemas	52014
Screw M6	16	-	-
Nut M6	24	-	-
Washer M6	24	-	-
Connection 90º Angle	8	Fasten Sistemas	5333
Threaded Bar M6	2 x 120mm	-	-

Tabla 6: Open Tunnel Set Up Inventory

Product Name	Qty.	Supplier	Product Reference
Basic profile 30x30mm, 8mm slot	3.09 [m]	Fasten Sistemas	5010
Hammer head nut	18	Fasten Sistemas	52014
Screw M6	18	-	-
Washer M6	18	-	-
Connection 90º Angle	8	Fasten Sistemas	5333

Tabla 7: Closed Tunnel Set Up Inventory

B Appendix II - Blueprints

Dimensions in millimetres [mm] unless otherwise specified.

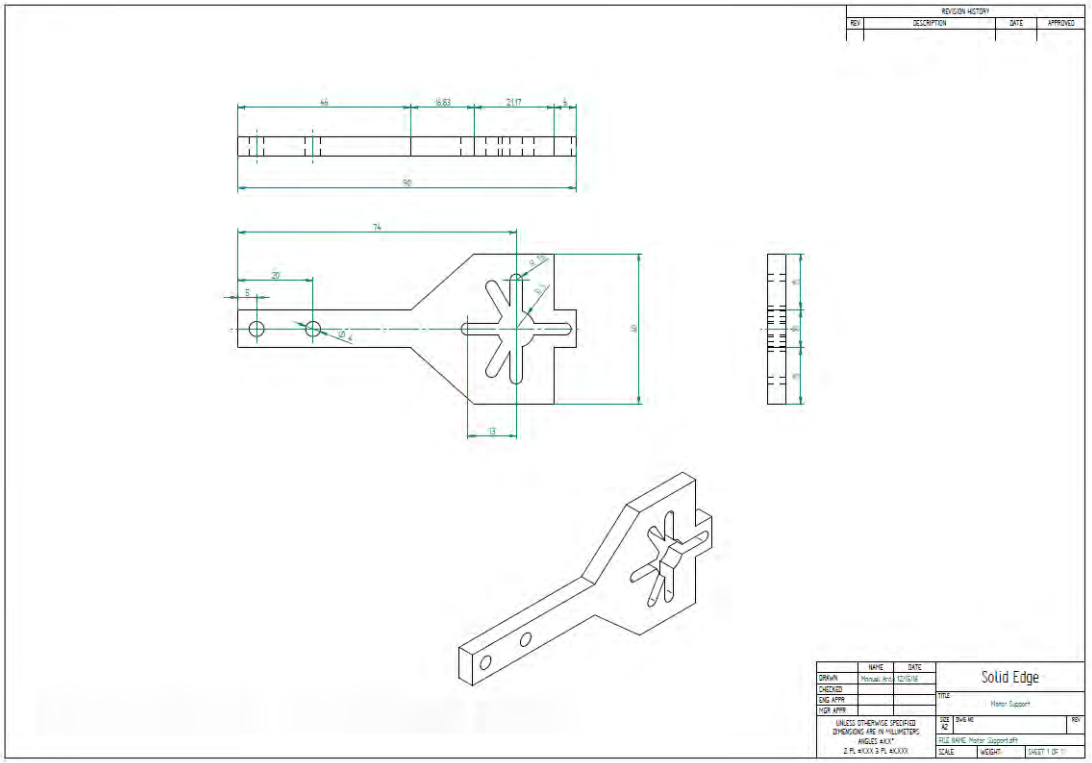

Figura 59: Motor Support Blueprint

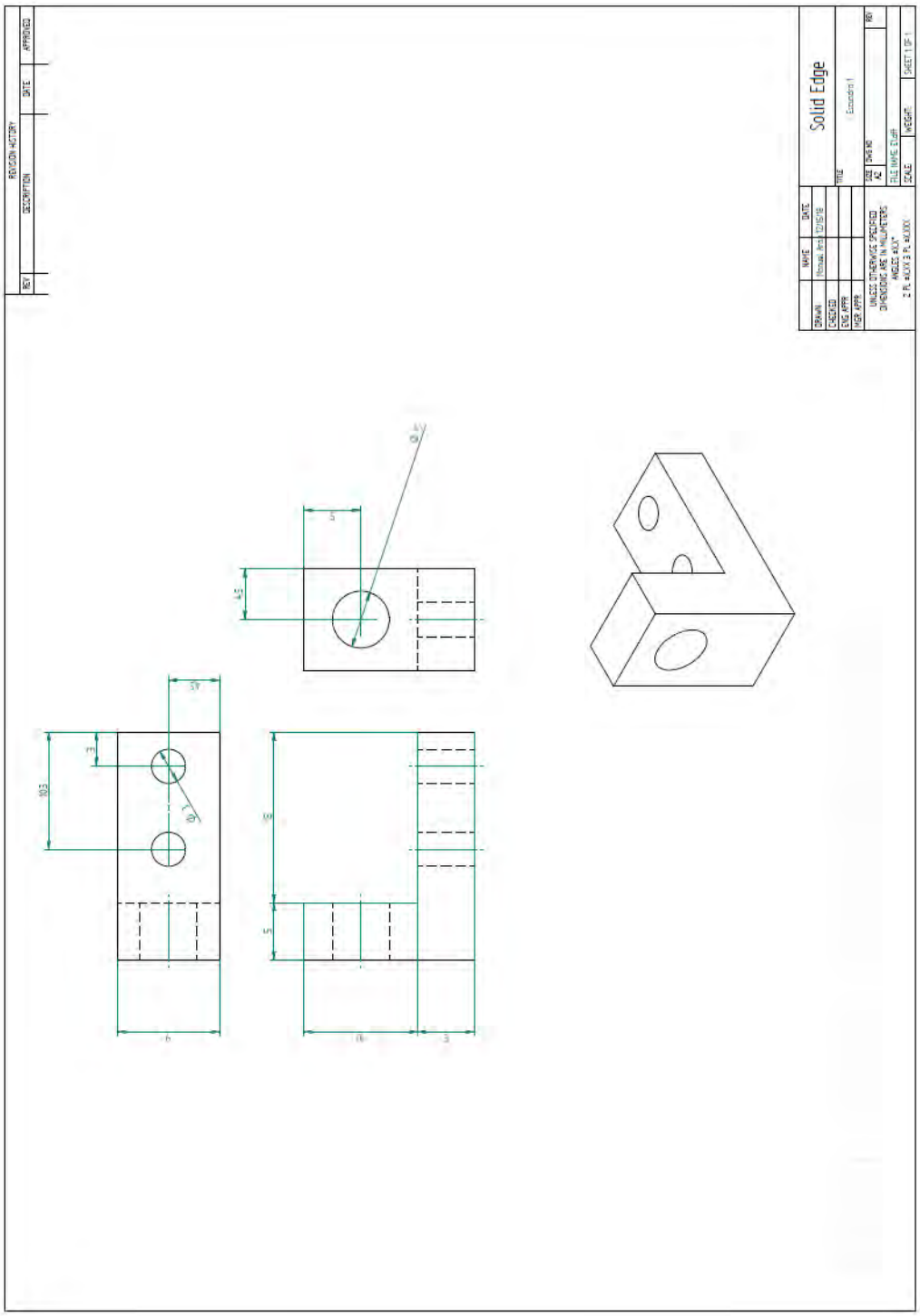

Figura 60: 90º Angle Connector Blueprint

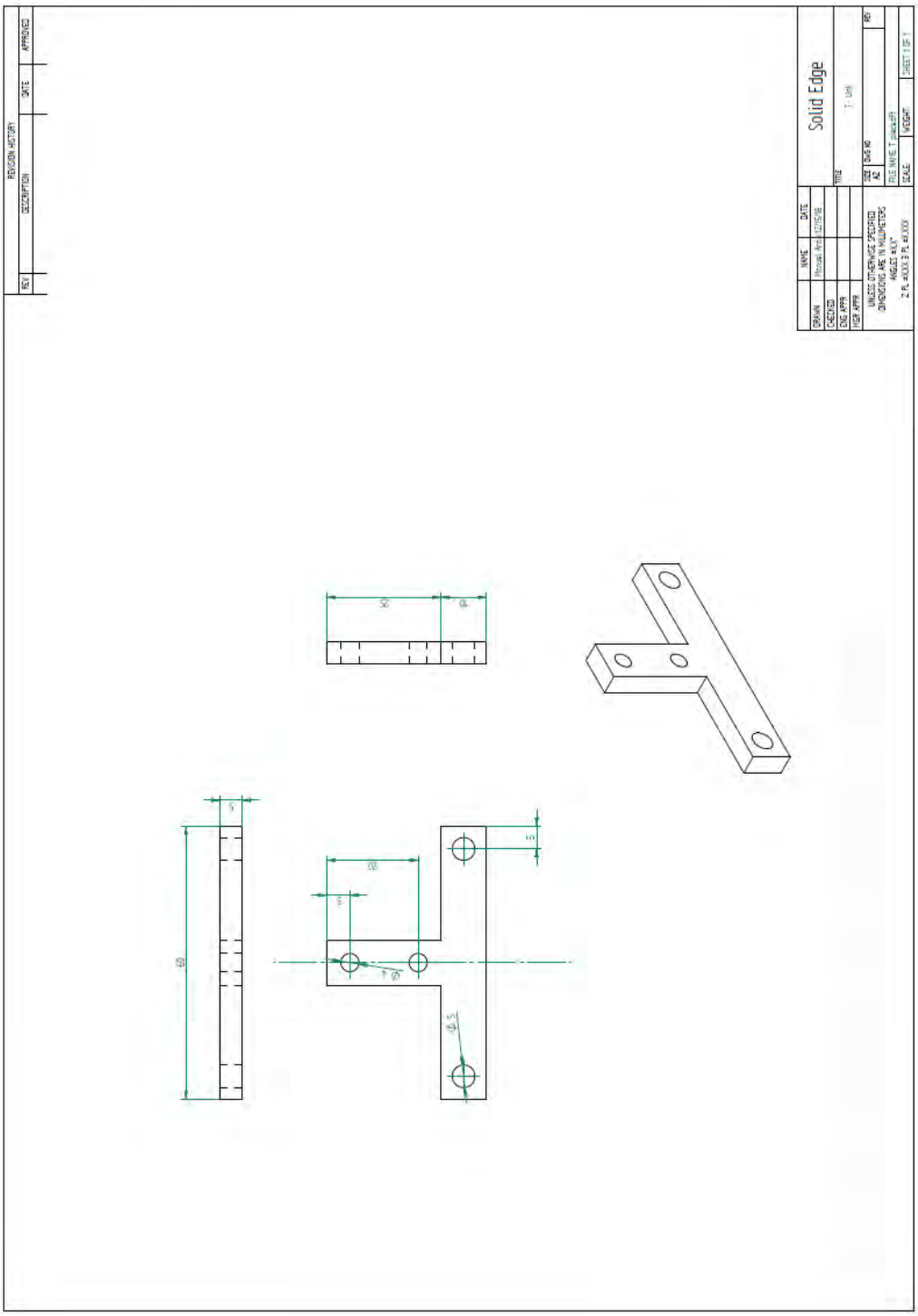

Figura 61: T-Link Blueprint

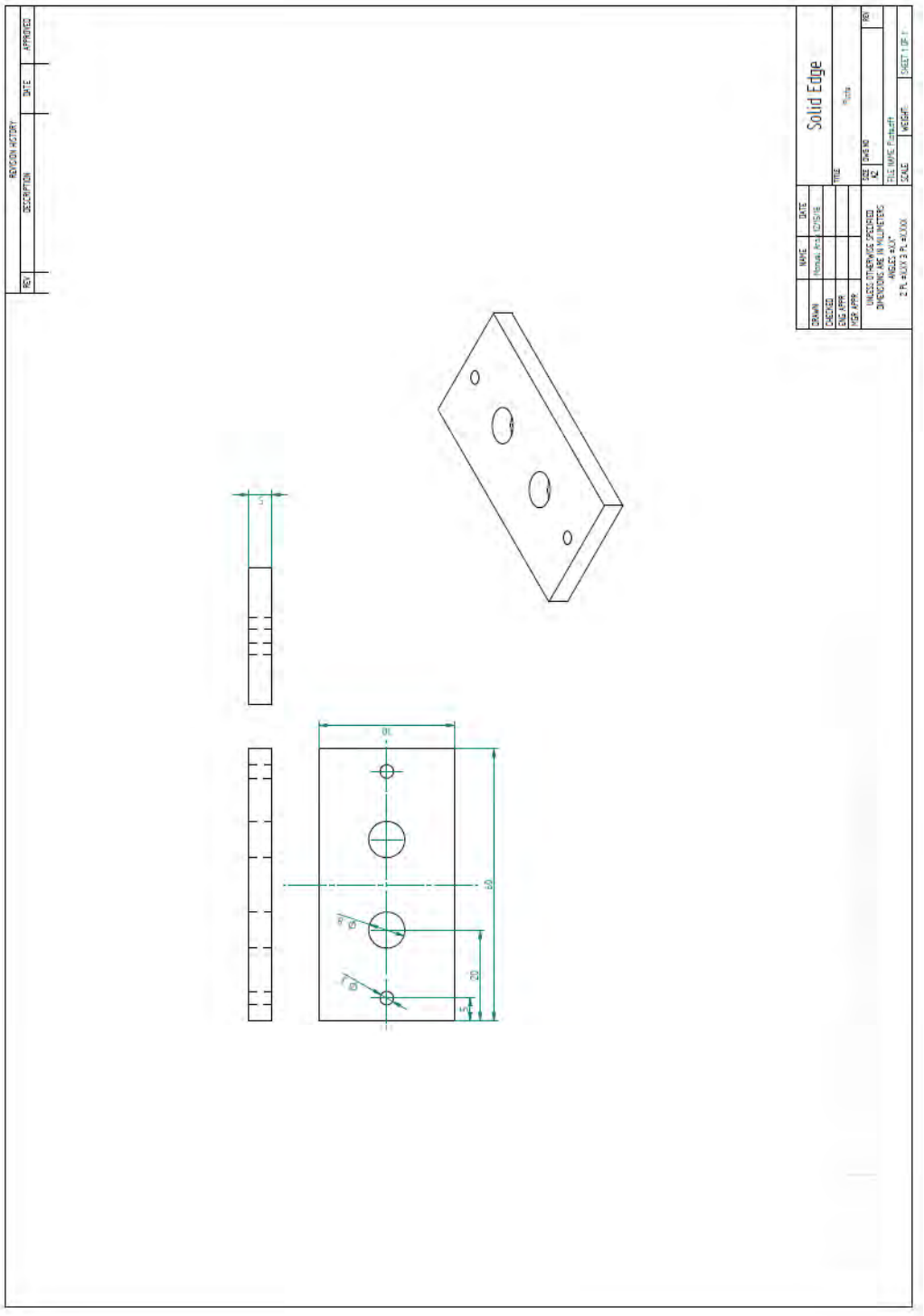

Figura 62: Slot Plate Blueprint

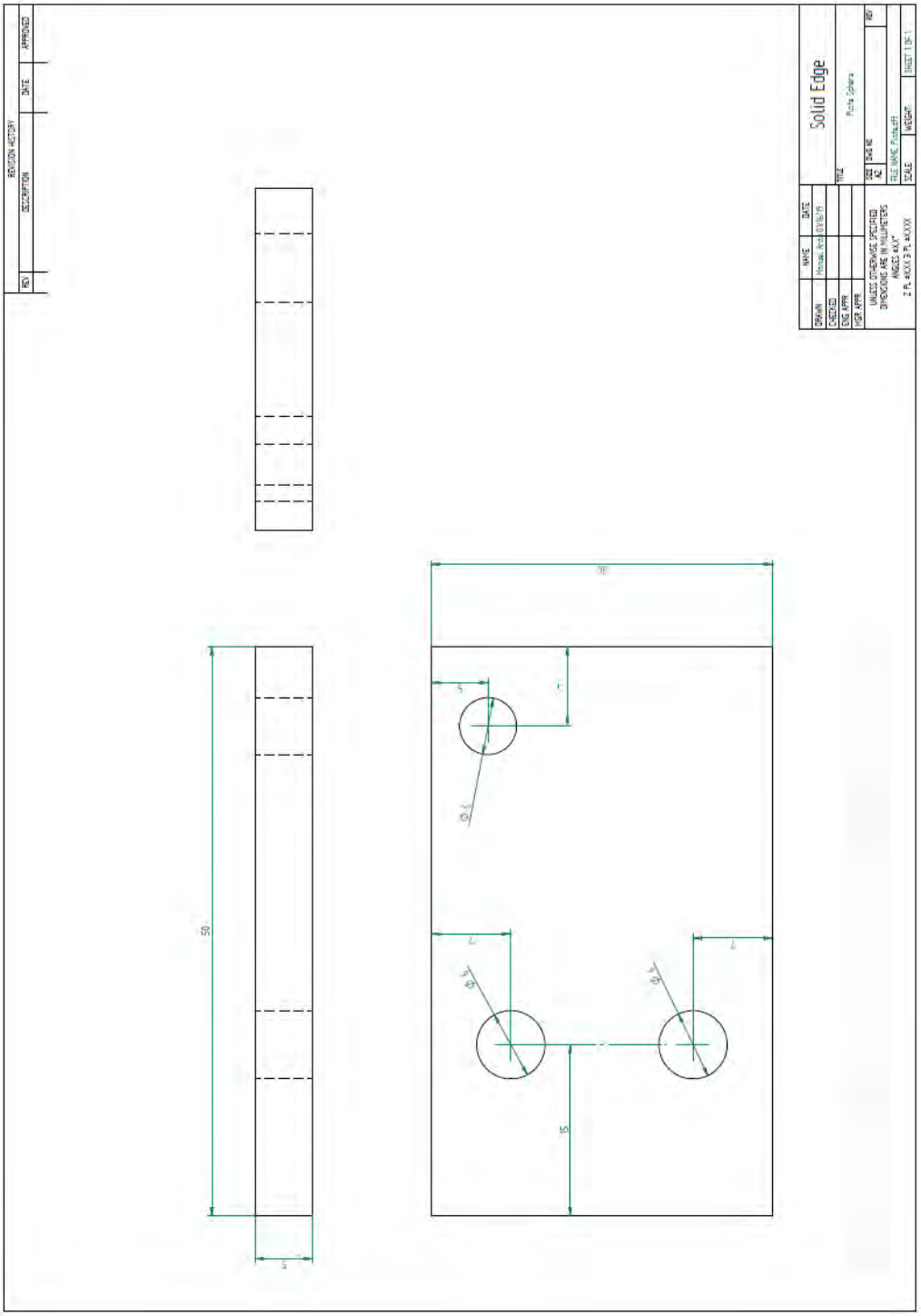

Figura 63: Plate Blueprint

C Appendix III - Performance Curves

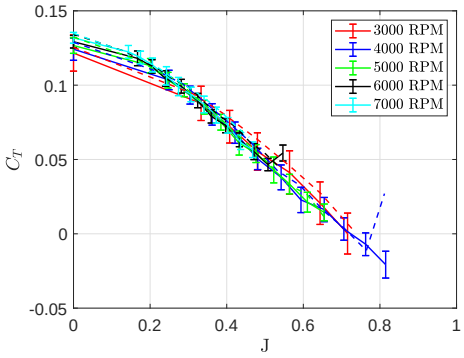

Figura 64: C_T vs J @ $\bar{D} = 0.25$ & $\bar{L} = 0.5$

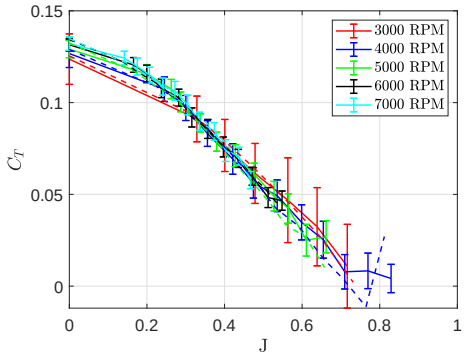

Figura 65: C_T vs J @ $\bar{D} = 0.5$ & $\bar{L} = 0.5$

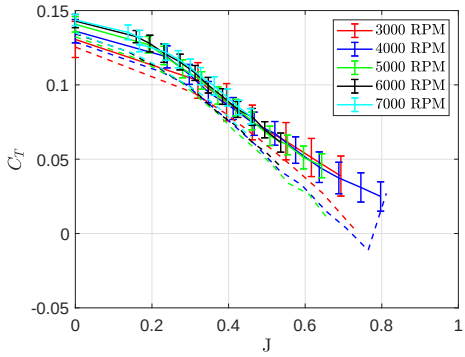

Figura 66: C_T vs J @ $\bar{D} = 0.75$ & $\bar{L} = 0.5$

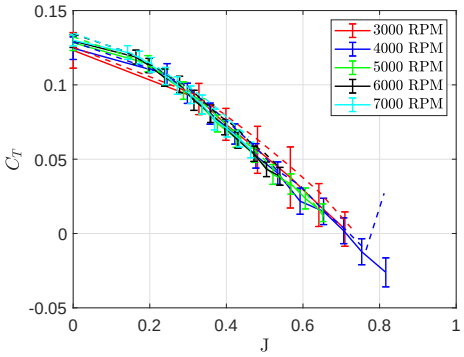

Figura 67: C_T vs J @ $\bar{D} = 0.25$ & $\bar{L} = 1$

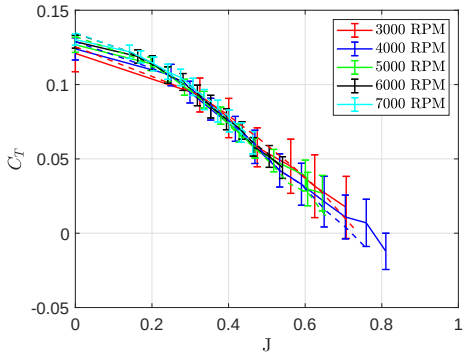

Figura 68: C_T vs J @ $\bar{D} = 0.5$ & $\bar{L} = 1$

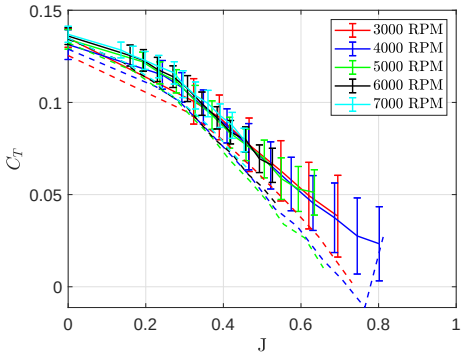

Figura 69: C_T vs J @ $\bar{D} = 0.75$ & $\bar{L} = 1$

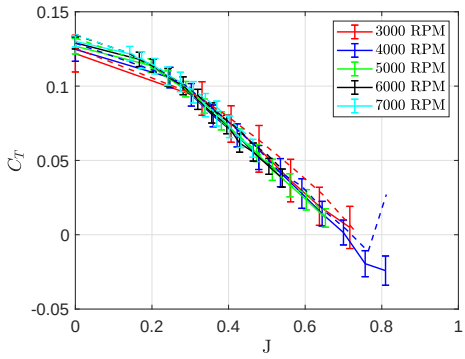

Figura 70: C_T vs J @ $\bar{D} = 0.25$ & $\bar{L} = 1.5$

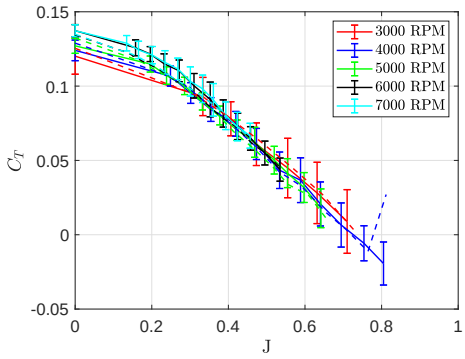

Figura 71: C_T vs J @ $\bar{D} = 0.5$ & $\bar{L} = 1$.

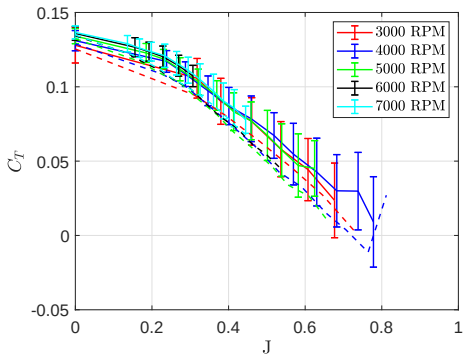

Figura 72: C_T vs J @ $\bar{D} = 0.75$ & $\bar{L} = 1.5$

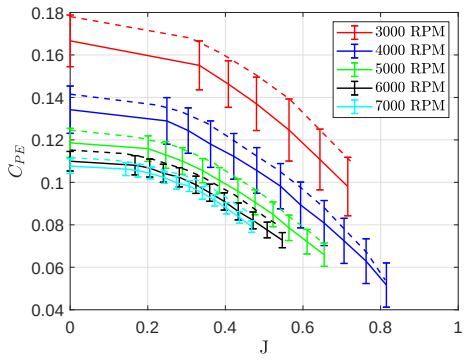

Figura 73: C_{PE} vs J @ $\bar{D} = 0.25$ & $\bar{L} = 0.5$

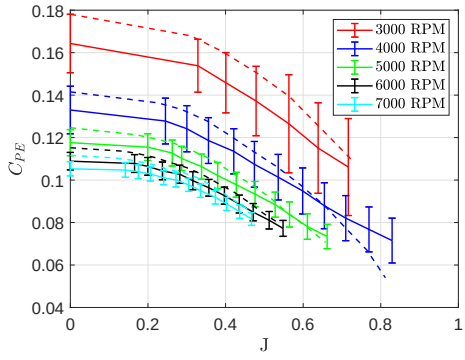

Figura 74: C_{PE} vs J @ $\bar{D} = 0.5$ & $\bar{L} = 0.5$

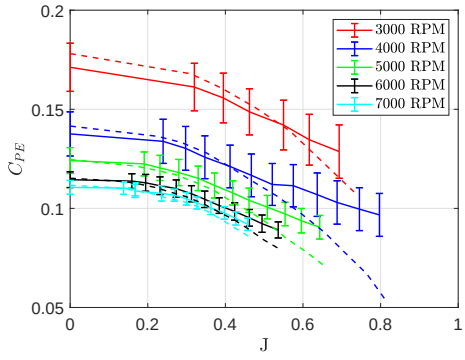

Figura 75: C_{PE} vs J @ $\bar{D} = 0.75$ & $\bar{L} = 0.5$

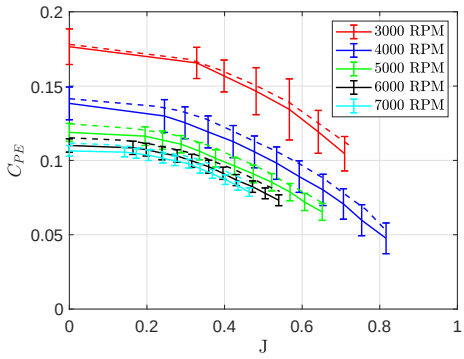

Figura 76: C_{PE} vs J @ $\bar{D} = 0.25$ & $\bar{L} = 1$

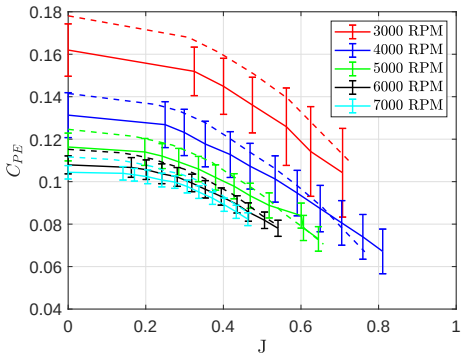

Figura 77: C_{PE} vs J @ $\bar{D} = 0.5$ & $\bar{L} = 1$

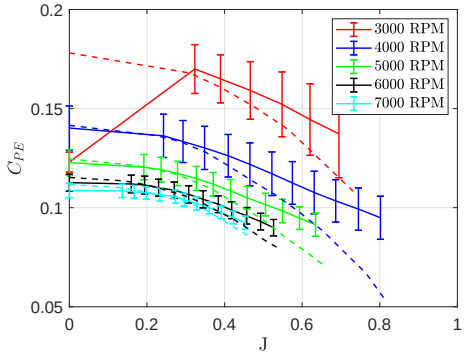

Figura 78: C_{PE} vs J @ $\bar{D} = 0.75$ & $\bar{L} = 1$

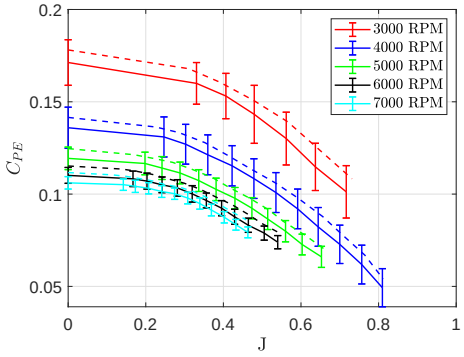

Figura 79: C_{PE} vs J @ $\bar{D} = 0.25$ & $\bar{L} = 1.5$

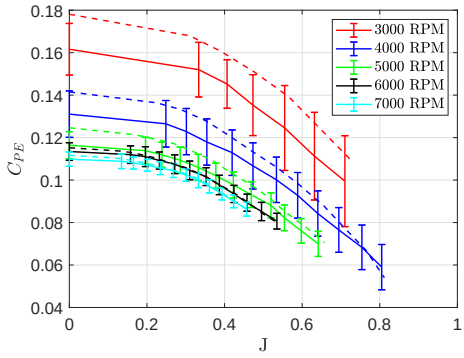

Figura 80: C_{PE} vs J @ $\bar{D} = 0.5$ & $\bar{L} = 1.5$

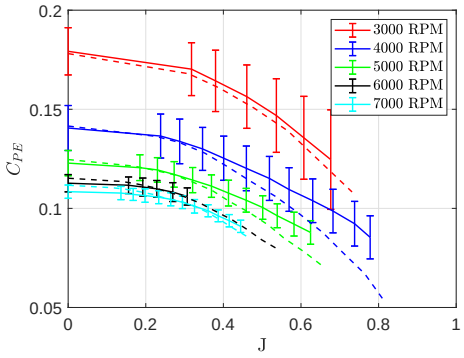

Figura 81: C_{PE} vs J @ $\bar{D} = 0.75$ & $\bar{L} = 1.5$

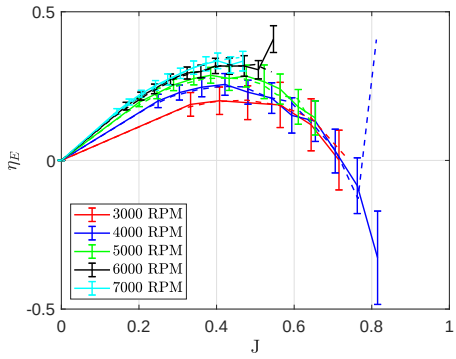

Figura 82: η_{PE} vs J @ $\bar{D} = 0.25$ & $\bar{L} = 0.5$

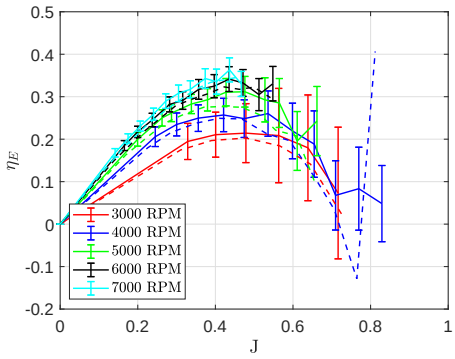

Figura 83: η_{PE} vs J @ $\bar{D} = 0.5$ & $\bar{L} = 0.5$

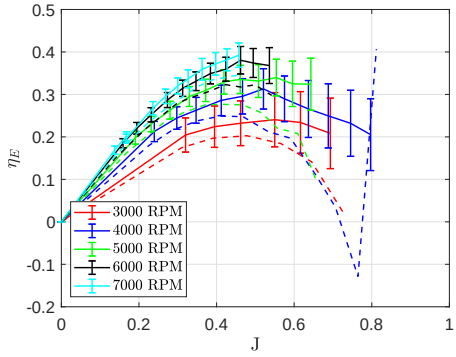

Figura 84: η_{PE} vs J @ $\bar{D} = 0.75$ & $\bar{L} = 0.5$

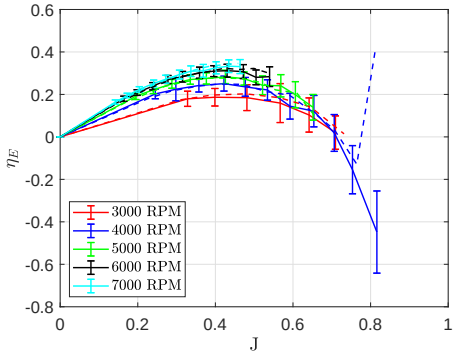

Figura 85: η_{PE} vs J @ $\bar{D} = 0.25$ & $\bar{L} = 1$

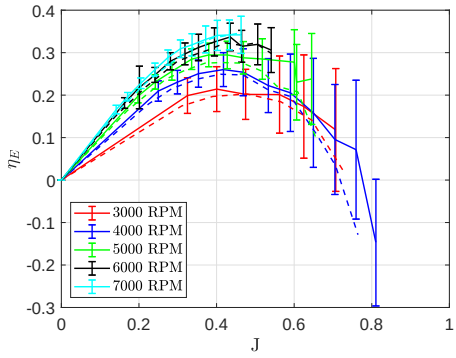

Figura 86: η_{PE} vs J @ $\bar{D} = 0.5$ & $\bar{L} = 1$

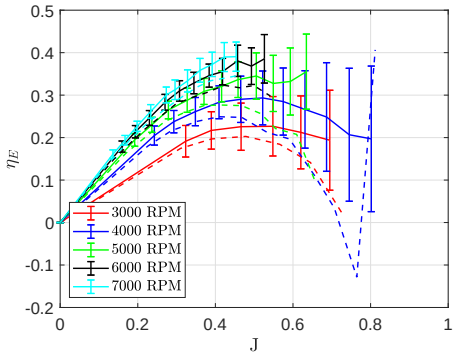

Figura 87: η_{PE} vs J @ $\bar{D} = 0.75$ & $\bar{L} = 1.5$

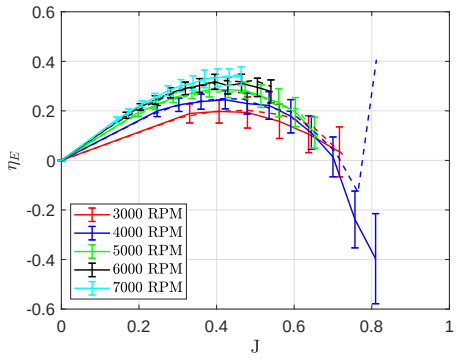

Figura 88: η_{PE} vs J @ $\bar{D} = 0.25$ & $\bar{L} = 1.5$

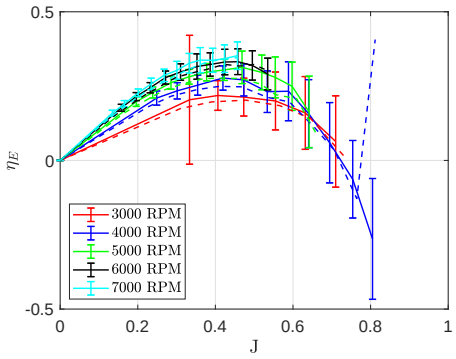

Figura 89: η_{PE} vs J @ $\bar{D} = 0.5$ & $\bar{L} = 1.5$

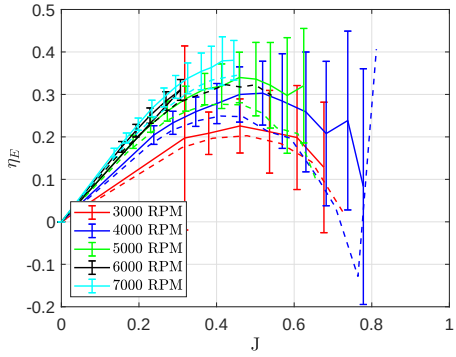

Figura 90: η_{PE} vs J @ $\bar{D} = 0.75$ & $\bar{L} = 1.5$

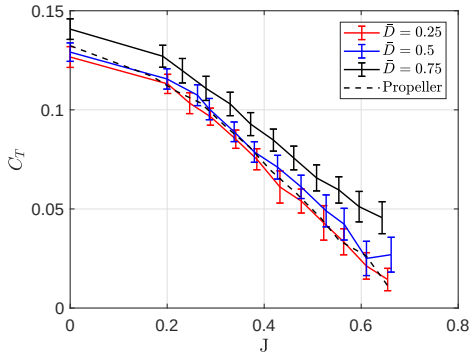

Figura 91: C_T vs J @ $\bar{L} = 0.5$

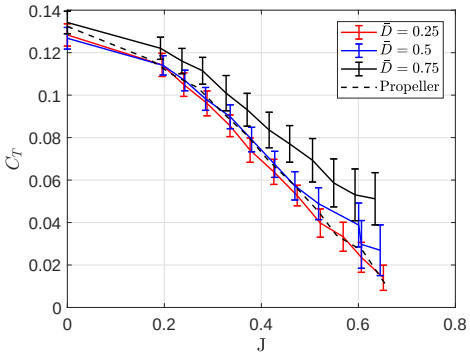

Figura 92: C_T vs J @ & $\bar{L} = 1$

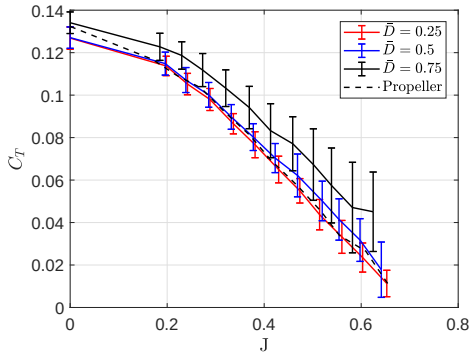

Figura 93: C_T vs J @ $\bar{L} = 1.5$

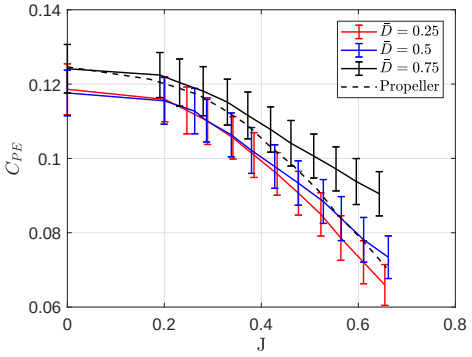

Figura 94: C_{PE} vs J @ & $\bar{L} = 0.5$

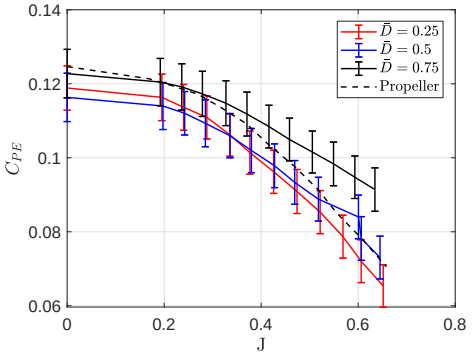

Figura 95: C_{PE} vs J @ $\bar{L} = 1$

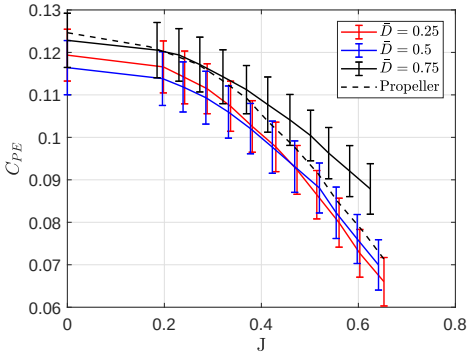

Figura 96: C_{PE} vs J @ & $\bar{L} = 1.5$

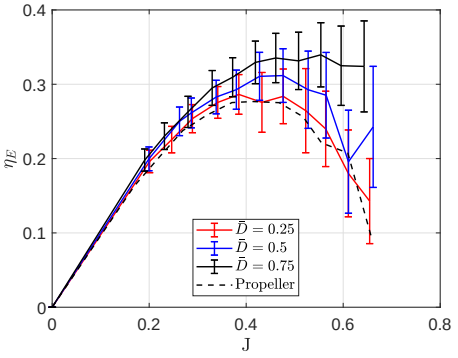

Figura 97: η_{PE} vs J @ $\bar{L} = 0.5$

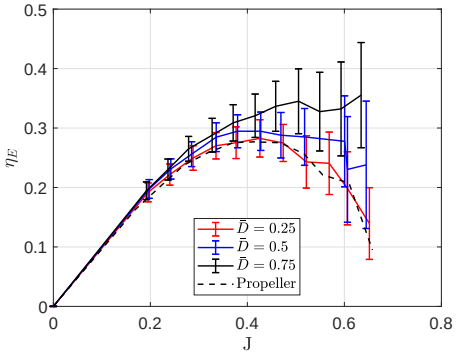

Figura 98: η_{PE} vs J @ & $\bar{L} = 1$

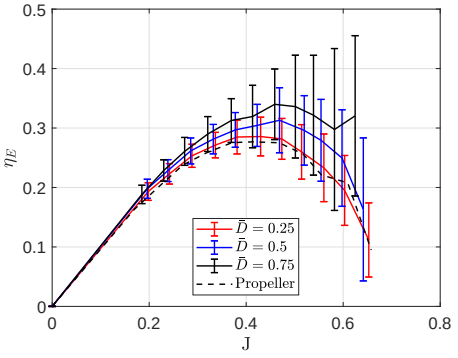

Figura 99: η_{PE} vs J @ $\bar{L} = 1.5$

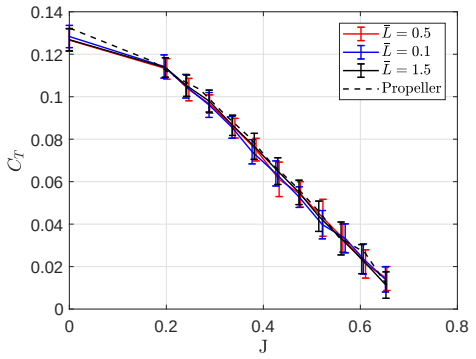

Figura 100: C_T vs J @ & $\bar{D} = 0.25$

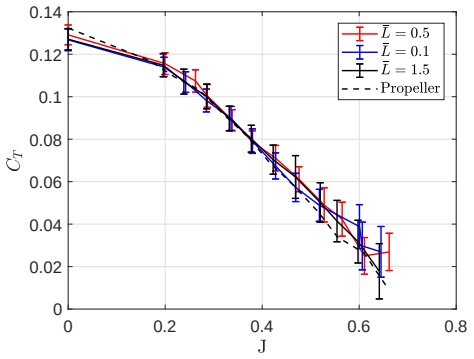

Figura 101: C_T vs J @ $\bar{D} = 0.5$

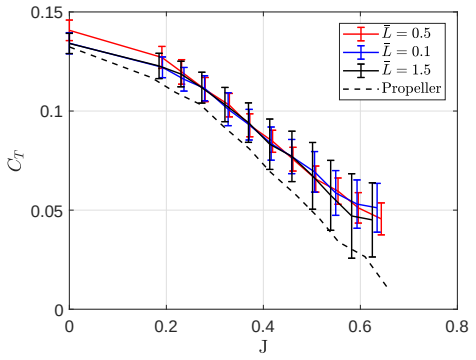

Figura 102: C_T vs J @ & $\bar{D} = 0.75$

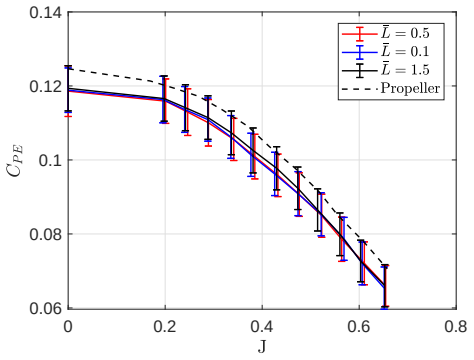

Figura 103: C_{PE} vs J @ $\bar{D} = 0.25$

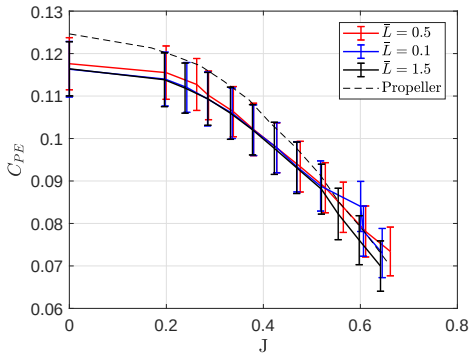

Figura 104: C_{PE} vs J @ & $\bar{D} = 0.50$

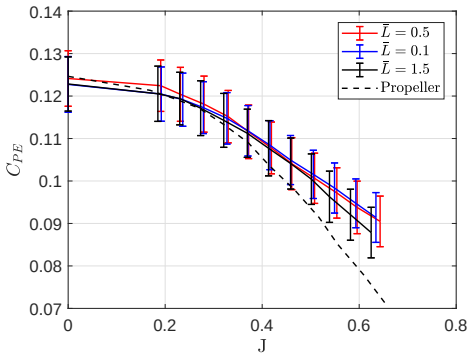

Figura 105: C_{PE} vs J @ $\bar{D} = 0.75$

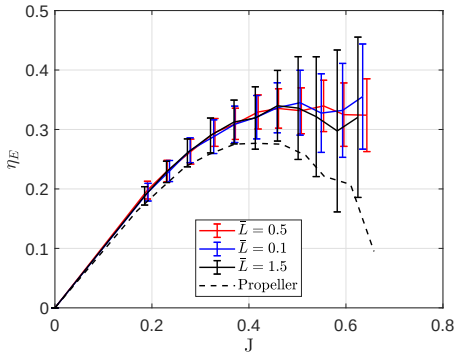

Figura 108: η_{PE} vs J @ $\bar{D} = 0.75$

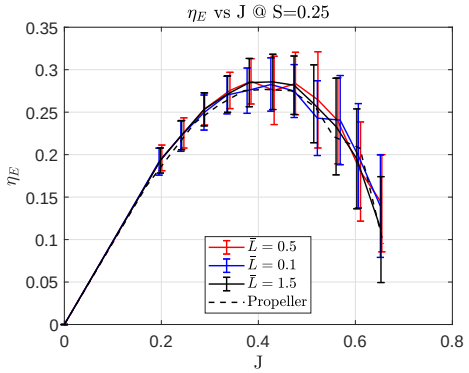

Figura 106: η_{PE} vs J @ & $\bar{D} = 0.25$

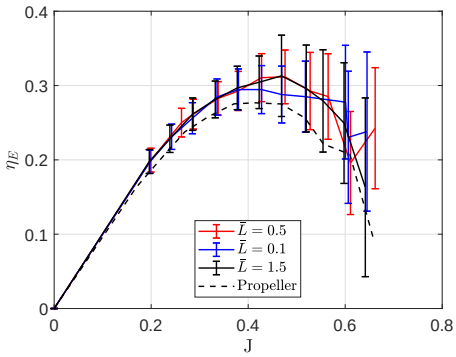

Figura 107: η_{PE} vs J @ $\bar{D} = 0.50$